J. metamorphic Geol., 1995, 13, 559–576

Strain-related differences in the crystal growth of white mica and chlorite: a TEM and XRD study of the development of metapelitic microfabrics in the Southern Uplands thrust terrane, Scotland

R. J. MERRIMAN,[1] B. ROBERTS,[2] D. R. PEACOR[3] AND S. R. HIRONS[2]
[1] British Geological Survey, Keyworth, Nottingham NG12 5GG, UK (email: k_rjm@ua.mkw.ac.uk)
[2] Birkbeck College, University of London, Malet Street, London WC1E 7HX, UK
[3] University of Michigan, Ann Arbor, MI 48109–1063, USA

ABSTRACT TEM and XRD techniques were used to study crystal growth characteristics of the fabric-forming phyllosilicates which developed in response to low-grade metamorphism and tectonic imbrication in part of the Southern Uplands thrust terrane. Prograde regional metamorphism, ranging from late diagenesis through the anchizone to the epizone, was accompanied by the development of a slaty cleavage which is commonly bedding-parallel. TEM-measured mean thicknesses of white mica and chlorite crystallite populations increase with advancing grade and correlate with XRD-measured crystallinity indices. Analytical TEM data show that prograde changes in composition lead to a net loss of Si, Ca and minor Fe from the fabric-forming phyllosilicates. White micas are paragonite-poor phengites with a mean *b* lattice parameter of 9.037 Å, and indicate an intermediate pressure series of metamorphism with a field gradient of <25° C km^{-1}. Chlorite compositions evolved from diabantite (with intergrown corrensite) to ripidolite over an estimated temperature range of 150–320° C. Field gradient and temperature estimates suggest that crystal growth and fabric development occurred at burial depths ranging from 6 km to at least 13 km in the thrust terrane. During late diagenesis, crystal growth of white mica and chlorite was predominantly a consequence of polytypic and phase transitions, and resulted in similar size distributions which resemble typical Ostwald ripening curves. Under anchizonal and epizonal conditions, white mica grew more rapidly than chlorite because of its greater ability to store strain energy and recover from subgrain development; as a result crystal thickness distributions are not typical of Ostwald ripening. In contrast, chlorite crystals which grew under these conditions developed subgrain boundaries at high strain rates which were only partially recovered at low strain rates; these retained dislocations reduce the crystallite thicknesses detected by TEM and XRD, compared with those of white mica. These differences in strain-induced crystal growth indicate that white mica (illite) and chlorite crystallinity indices are likely to show significant differences where low-grade metamorphism is closely associated with tectonic fabric development.

Key words: chlorite; crystallinity; crystal size; mica *b* parameter; phengite; tectonic strain.

INTRODUCTION

Although slate was one of the first rocks studied with the petrological microscope (Sorby, 1853), the nature of the phyllosilicates in slate and many other fine-grained rocks had to await the application of X-ray diffraction techniques (XRD) in the 1920s and onwards. The subsequent application of transmission electron microscopy (TEM) revealed the detail of slaty cleavage microstructure developed predominantly in phyllosilicate-rich rocks, and the interdependence of deformation and metamorphic crystallization processes involved in its development (e.g. White & Knipe, 1978; Knipe, 1981). These TEM studies indicated that the early stages of development are largely a response to mechanical deformation, while at a later stage grain orientation, composition, strain rates and crystallization processes are interactive (Knipe, 1981). When they are deformed, the phyllosilicates involved in these processes respond by intracrystalline deformation. In some cases the resulting strain-induced dislocations form subgrain boundaries and this causes crystal size reduction (polygonization/segmentation), whereas in other cases subgrain and grain boundaries migrate and this may result in larger crystals (e.g. Wilson & Bell, 1979; Bell & Wilson, 1981; Bons, 1988). However, the crystal size of phyllosilicates generally increases as grade and the intensity of cleavage development increases across regionally metamorphosed terranes. Hence the progressive thickening of white mica crystals is the basis of the illite crystallinity technique and its use as an indicator of

metapelitic grade (Frey, 1987, and references therein; Merriman *et al.*, 1990; Warr & Rice, 1994).

Despite recognition of the importance of elastic and plastic strain energies in metamorphic crystal growth (Atherton, 1976; Rietan, 1977), in the case of phyllosilicates relationships between strain, intracrystalline deformation and phyllosilicate crystal growth during metamorphism remain unclear (e.g. Frey, 1987, pp. 18–19). Nevertheless, several TEM studies contrasting the response of different phyllosilicates to deformation provide important signposts. For example, Bell & Wilson (1981) found that the density of defects in biotite increased with strain whereas associated muscovite showed no comparable increase. These two micas also behaved differently during shearing experiments, with biotite dislocations proving much easier to activate than those of muscovite (Meike, 1989). During slaty cleavage development, Bons (1988) found that chlorite crystals deformed by intracrystalline slip and subgrain development, causing polygonization, while white mica crystals appeared to have a greater capacity to store plastic and elastic strain energy, and grow by grain-boundary migration. These studies suggest that, despite having similar layer silicate structures, intergrown phyllosilicates could be expected to show different crystal growth rates and degrees of crystal perfection as a result of deformation and metamorphism.

Whereas scanning electron microscopy (SEM), especially using back-scattered imaging (BSI), has led to progress in the understanding of cleavage development at the microscopic level, the technique yields no information on intracrystalline nanotextures. We have therefore used a combination of TEM and XRD techniques to study intracrystalline phenomena associated with crystal growth of white mica and chlorite in response to low-grade metamorphism and tectonic fabric development. Details of the textures, crystallite size distribution and composition of fabric-forming phyllosilicates are presented and we show that tectonic strain played an important part in their development. We also studied the relationship between the XRD-measured crystallinity index of white mica and chlorite and the TEM-measured crystallite thickness, and show that these measurements can be correlated.

METAMORPHIC GEOLOGY AND SAMPLES

The samples studied are part of a suite of mudrocks (mudstones, shales and slates) collected from Lower Palaeozoic strata of the Southern Uplands of Scotland where they comprise an imbricate thrust terrane which developed during closure of the Iapetus ocean (McKerrow, 1987, and references therein). The Lower Palaeozoic succession is dominated by thick sequences of turbidite sandstones with thin shaly partings, and they are commonly underlain by graptolitic black and grey shales, the Moffat Shale Group, up to 100 m in thickness. Faunas in the shales provide the biostratigraphy shown in Fig. 1. Vertical or steeply inclined strike-parallel faults, trending NE–SW, divide the area into a series of major slices or tracts. Within each fault-bounded tract the beds are predominantly steeply dipping or vertical and mostly young to the north-west. However, the succession comprising each tract overall becomes sequentially younger to the south-east (Fig. 1).

Previous studies of regional metamorphism across the Southern Uplands showed that the prehnite–pumpellyite facies is widely developed in volcaniclastic turbidites and scarce metabasic volcanic rocks (Oliver & Leggett, 1980). White mica (illite) crystallinity, mica *b* lattice parameters (sometimes referred to as b_0) and graptolite reflectance data derived from samples from several traverses across the terrane indicate mostly anchizonal and late diagenetic grades in pelitic rocks (Oliver *et al.*, 1984; Kemp *et al.*, 1985). As part of the current reinvestigation of the Southern Uplands by the British Geological Survey, white mica crystallinity surveys, based on a sampling density of 1 mudrock sample per 2–3 km^2, have closely followed geological mapping of areas in the south-west of the terrane.

In one of these areas, the Rhins of Galloway, detailed tectonostratigraphic control allowed the crystallinity survey and the resulting contoured metamorphic map (Fig. 2) to be closely linked with the revised structure and stratigraphy (British Geological Survey, 1992). The metamorphic survey determined the <2-μm mineral assemblages and white mica crystallinity (Kübler indices, *KI*) of 200 mudrock samples by XRD (Merriman & Roberts, 1993), using the machine and measuring conditions detailed in Roberts *et al.* (1991). Lowest grade late diagenetic zone mudstones and shales consist of chlorite with subordinate illite and corrensite and minor amounts of kaolinite, mixed-layer illite/smectite, albite, quartz and hematite. Illite shows broad, generally symmetrical 10-Å peaks with *KI*s in the range 0.42–0.66 $\Delta°2\theta$. Shales and slates of anchizonal grade are typically composed of chlorite and phengitic $2M_1$ K-mica with *KI*s in the range 0.25–0.42 $\Delta°2\theta$; minor albite and quartz are also present, but corrensite and paragonite are absent. Highest grade epizonal slates contain $2M_1$ K-mica ($KI < 0.25$ $\Delta°2\theta$) and chlorite, with minor albite, quartz and rutile. Variations in the range and mean *KI* for each of the major tectonostratigraphic units on the Rhins of Galloway are shown in Fig. 1.

The regional development of a tectonic fabric in the pelitic rocks is closely linked with metapelitic grade. In lowest grade, late diagenetic mudstones and shales, a fabric is either absent or very weakly developed as an impersistent spaced cleavage. A cleavage is developed in anchizonal pelites, but is commonly bedding-parallel or at a low angle (<20°) to bedding and for this reason easily mistaken for a shaly fissility. Thin sections show that the microfabric consists of anastomosing intergrowths of orientated white mica and chlorite, approximately parallel to bedding lamination, representing the recrystallized clay matrix of the original mudstone. In the lower anchizone (*KI* 0.30–0.42), the thickness of the orientated intergrowths comprising the microfabric P-domains (Knipe, 1981) rarely exceeds 2 μm whereas detrital micas in the

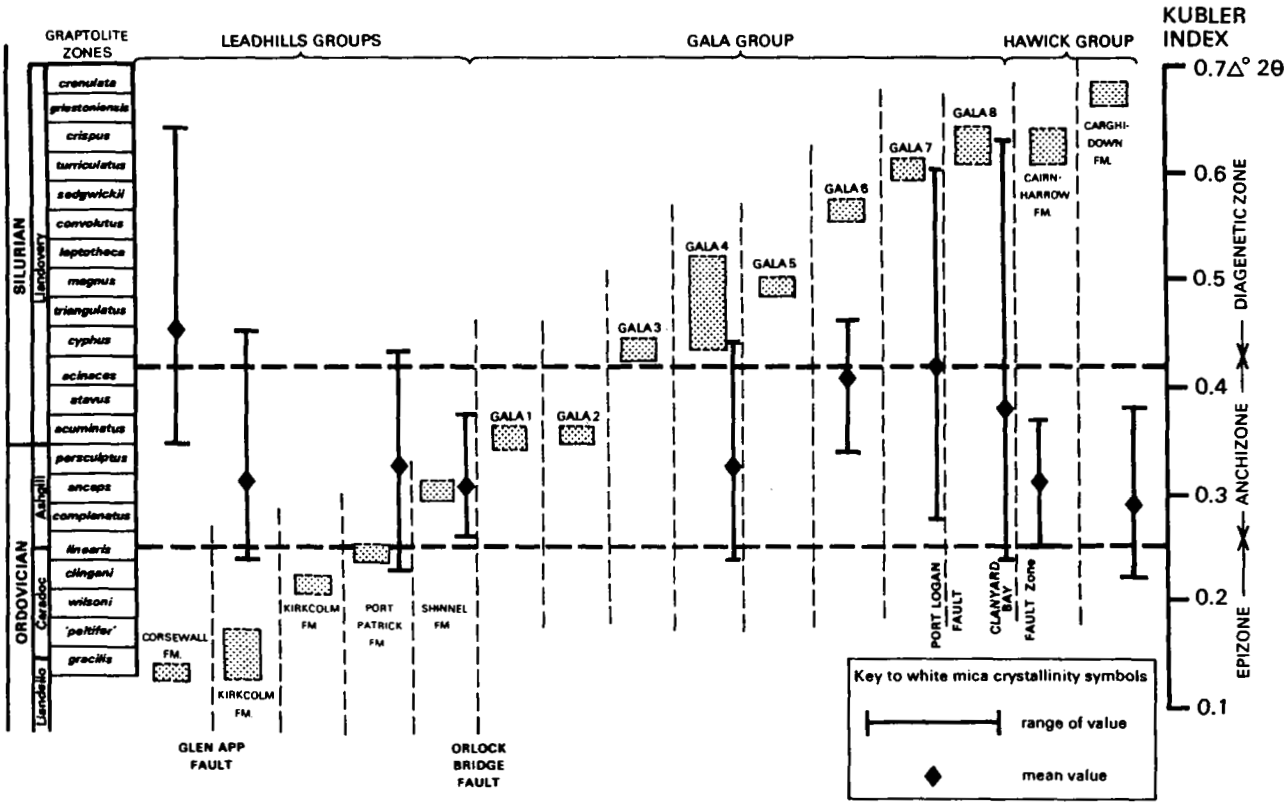

Fig. 1. Simplified biostratigraphical chart of the Rhins of Galloway (Rushton & Tunnicliff in Stone, 1995), showing the mean and range of white mica crystallinity (Kubler) indices for the main tectonostratigraphic units. The stippled boxes show the age range of the greywackes in each unit.

same orientation are generally two or three times thicker (Fig. 3B). In the upper anchizone (*KI* 0.25–0.30) and epizone, a conspicuous continuous cleavage is developed in both pelites and associated greywacke sandstones. P-domains of the microfabric are significantly thicker, and comparable in width with all but the thickest detrital micas and chlorite–mica stacks (Fig. 3C).

The three samples selected for high-resolution transmission electron microscopy and analytical electron microscopy (HRTEM/AEM) are representative both of the metamorphic zones shown in Fig. 2 and of the progressive development of the tectonic fabric.

Sample BRS 429 is a late diagenetic mudstone from the Corsewall Formation (Fig. 1; Llandeilo–Caradoc, *gracilis* biozone), cropping out at Corsewall Point [NW 9911 7257]. The dark grey-green, laminated silty mudstone is interbedded with sandstones and conglomerates dipping steeply to the NW and striking at 068°. In parts of the outcrop the mudstones show a poorly developed spaced cleavage, dipping less steeply than bedding. A back-scattered electron image (BSEI) of a thin section shows silt-sized grains of quartz, albite, K-feldspar, biotite flakes, magnetite and rare chromite, in a phyllosilicate matrix which lacks an obvious fabric (Fig. 3A). XRD analysis of the <2-μm fraction shows that the matrix consists of chlorite with subordinate corrensite and illite; minor amounts of kaolinite and hematite were identified by M. Frey (pers. comm.). Typically, corrensite shows a very low angle reflection at ≈28 Å which expands to 31–33 Å after glycerol saturation. The illite shows a broad but symmetrical 10-Å peak with a mean *KI* of 0.66 Δ°2θ, which is the highest value, i.e. lowest grade, found in the Corsewall Formation.

Sample BRS 444 is an achizonal slate from the Shinnel Formation (Fig. 1; Ashgill, *anceps* biozone), collected from outcrops about 3.5 km SE of Portpatrick [NX 0290 5224]. The blue-grey slate, with approximately bedding-parallel cleavage, forms thin (<30-cm) beds between steeply dipping, massive greywacke sandstone beds which strike at 073° and young towards the NNW. A BSEI of the slate shows a strongly developed bedding-parallel fabric of an orientated matrix of phyllosilicate intergrowths anastomosing around abundant albite and detrital mafic phyllosilicates, minor quartz, TiO_2 grains and apatite (Fig. 3B). XRD analysis shows that the intergrowths consist of abundant chlorite, subordinate white mica and minor albite; neither corrensite nor paragonite are detectable. The 10-Å white mica peak gives a mean *KI* of 0.34 Δ°2θ.

Sample BRS 106 is a green slate of epizonal grade from the Carghidown Formation (Fig. 1; Llandovery, *greistoniensis–crenulata* biozones). It was collected from outcrop behind the Mull of Galloway lighthouse [NX 1568 3042], where a sequence of thinly bedded, carbonate-cemented sandstone

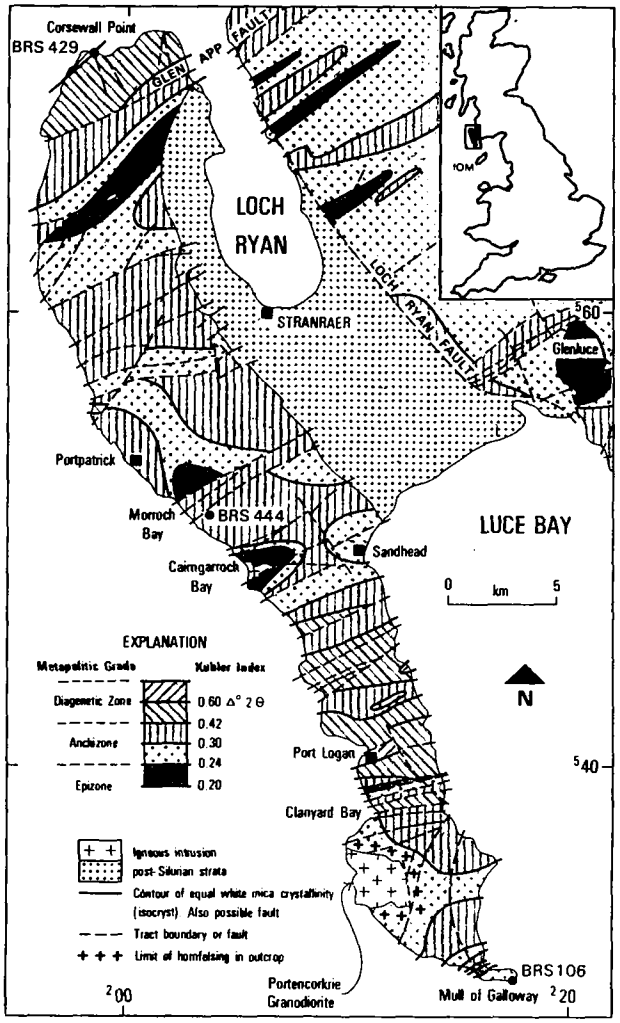

Fig. 2. Contoured metamorphic map of the Rhins of Galloway based on white mica crystallinity (Kubler) indices from 200 samples and a sampling density of approximately 1 mudrock per 2.5 km^2. BRS numbers give the location of the samples described in the text. Inset: the location of the Rhins of Galloway and the Isle of Man (IOM).

and plane-laminated silty slate beds youngs toward the NW; bedding is vertical, striking at 056°, and a vertical slaty cleavage strikes at 074°. A BSEI of the slate shows anastomosing cleavage domains enclosing grains of quartz, albite and detrital phyllosilicates, including chlorite/mica stacks (Fig. 3C). Some BSEI images (not shown) display orientated TiO_2 pseudomorphs that appear to represent original heavy mineral-rich laminae. XRD analysis of the <2-μm fraction indicates that $2M_1$ white mica and chlorite are the dominant phyllosilicates, with minor albite, quartz and rutile. The 10-Å white mica peak gives a mean *KI* of 0.23 $\Delta°2\theta$.

TRANSMISSION ELECTRON MICROSCOPY

Samples were prepared as sticky-wax mounted thin sections orientated approximately normal to the dominant planar fabric, following the methods used by Ahn & Peacor (1986). Carbon-coated thin sections were examined by optical microscopy and scanning electron microscopy (Fig. 3), to define suitable areas for TEM study. An aluminium washer was glued to the areas selected for study and these were then detached from the thin section, ion-milled and carbon-coated. Lattice-fringe images were obtained using a Philips CM 12 scanning-transmission electron microscope (STEM) fitted with a Kevex Quantum solid-state detector and computer system. The STEM was operated at 120 kV and a beam current of $\approx$20 μA, and most images were acquired at 120×10^3 or 160×10^3 magnification with an objective aperture of 20 μm diameter. A camera length of 770 mm and selected-area aperture of 10 μm diameter were used to acquire electron diffraction (SAED) patterns. Quantitative chemical analyses were acquired by EDX using a beam diameter of 50 Å and a scanning area of up to 90 000 Å^2. Muscovite, clinochlore, albite, fayalite and titanite were utilized to correct EDX data for unknowns by the thin-film method of Lorimer & Cliff (1976).

Lattice-fringe images

A TEM image of typical textures present in the matrix of the diagenetic mudstone sample BRS 429 is shown in Fig. 4(A). Subparallel packets of 14-Å chlorite and 10-Å phengitic mica are closely intergrown, with chlorite the dominant phase throughout. The white mica crystals are small, typically 50–250 Å thick, and commonly occur as dispersed packets comprising 1–3 crystallites. Small crystal size usually resulted in non-definitive SAED patterns from the white micas, but when b^*–c^* or pseudohexagonal equivalent sections were imaged these proved to be two-layer (2M) polytypes.

Both phyllosilicates show discrete areas of mottling, some of which are the result of beam damage. Other areas of variable contrast are kinks associated with nanometric-scale folds. Accommodation in the chlorite packets forming the core of the fold seen at the top of Fig. 4(A) has been achieved by intracrystal slip along dislocations parallel to (001). The kinks associated with the dislocations resemble the strain fields recorded in chlorite by Bons (1988) and also the dislocation fronts produced in mica by experimental shearing (Meike, 1989). Kinked chlorite and mica packets are a common feature of the TEM images of sample BRS 429, but unlike the microkinks found by Knipe (1981) they are not associated with slaty cleavage microstructure. However, these nanometric folds suggest that, despite the absence of an obvious tectonic fabric, a cryptic pervasive disruption has affected the mudstone matrix, and it is assumed to be related to early bedding imbrication, as discussed later. Many chlorite packets show areas of variable lattice-fringe periodicities along which fissures due to beam damage commonly develop. Detailed inspection of these areas reveals an interstratification of 14 Å layers with layers 10–12 Å thick. The 10–12-Å fringes invariably occur as single layers in sequences of 14-Å

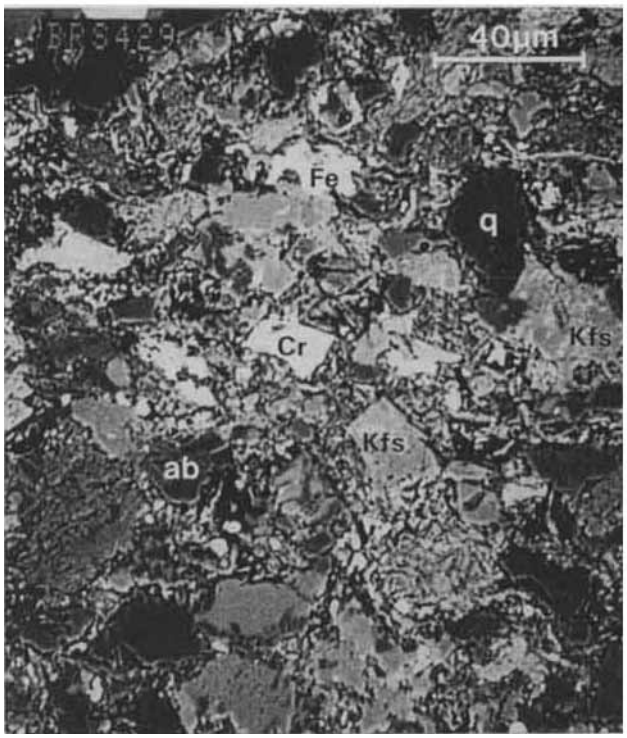

A

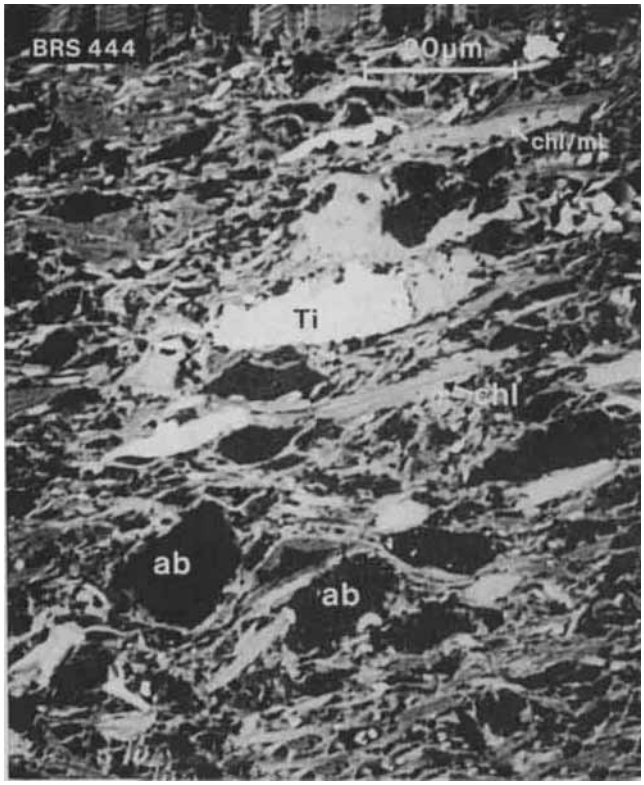

B

C

Fig. 3. Back-scattered electron images of the samples from the Rhins of Galloway. (A) Late diagenetic mudstone sample BRS 429; angular grains of quartz (q), albite (ab), K-feldspar (Kfs), magnetite (Fe), and minor chromite (Cr) and biotite flakes are contained in a matrix of intergrown chlorite, illite and corrensite. (B) Anchizonal slate sample BRS 444; grains of albite (ab), anatase (Ti) and detrital micas (mi), completely or partially altered to chlorite (chl), are crudely aligned in a bedding-parallel fabric. Anastomosing intergrowths of chlorite and phengite crystallites form a discontinuous bedding-parallel cleavage. (C) Epizonal slate sample BRS 106; grains of quartz (q), albite (ab), detrital mica (mi) and chlorite (chl)–mica stacks are enclosed in orientated intergrowths of phengite and chlorite, forming a continuous cleavage.

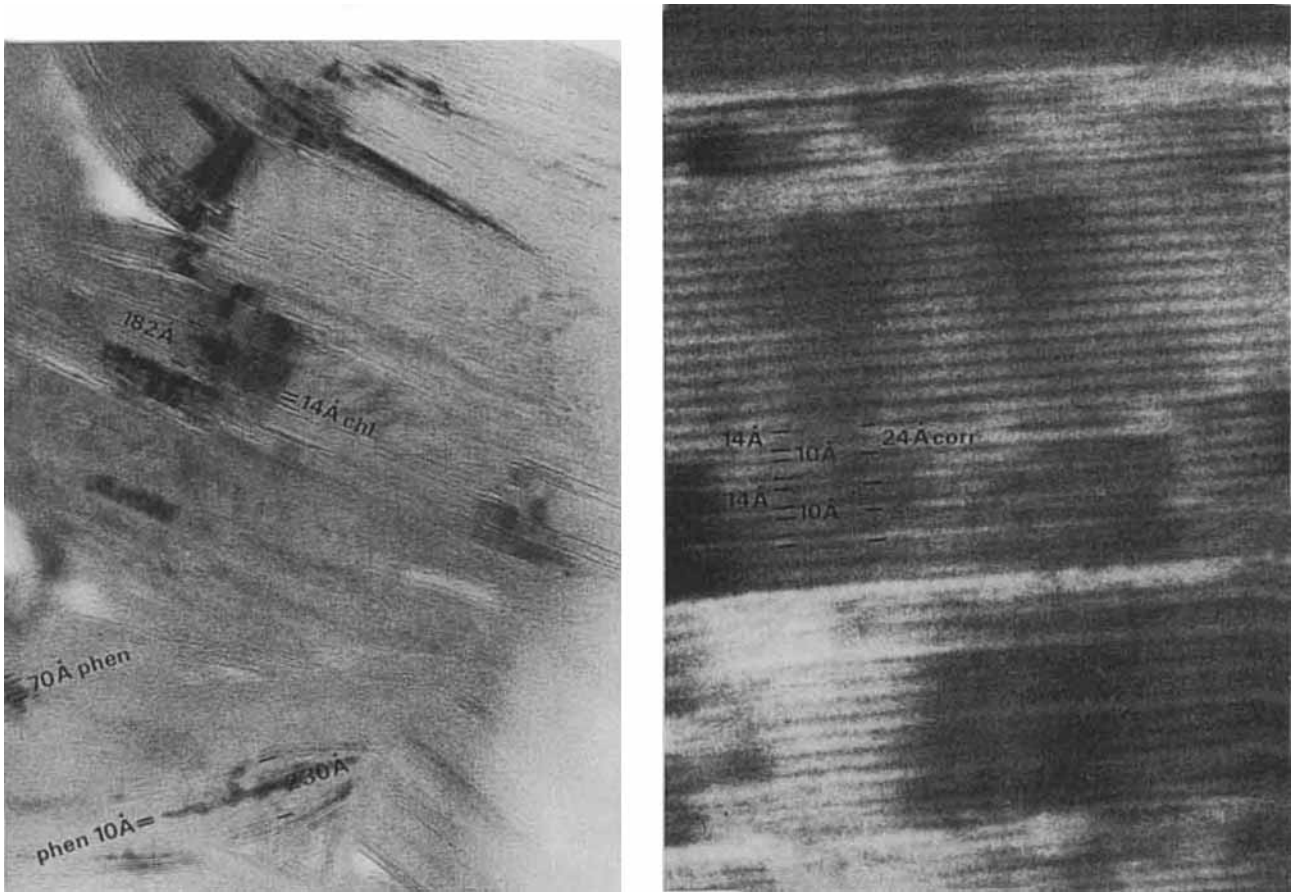

A B

Fig. 4. TEM lattice fringe images of matrix phyllosilicates in late diagenetic zone mudstone sample BRS 429. (A) Subparallel packets of chlorite (chl) and dispersed packets of phengitic white mica (phen); kinked chlorite fringes in the hinge of the nanometric-scale fold represent dislocations resulting from slip along (001). (B) Corrensite (corr) consisting of regular interstratification of 14-Å chlorite and 10-Å collapsed smectite within a packet dominated by 14-Å chlorite layers.

layers, and commonly transform to 14-Å layers parallel to (001). Regular interstratifications with a periodicity of ≈24 Å appear to be restricted to five or less repetitions within packets of 14-Å chlorite (Fig. 4B), similar to the occurrence of corrensite recorded by Shau *et al.* (1990) and Bettison-Varga *et al.* (1991). Thus the 10–12-Å layers are probably the expandable smectite layers identified by XRD, which have collapsed by dehydration in the electron beam.

TEM images of the matrix of the anchizonal slate BRS 444 show intergrowths of chlorite and phengitic mica that are coarser than those found in the diagenetic mudstone; they also show a greater density of nanometric-scale folds and intracrystalline deformation textures. Isolated 10–12-Å layers occur as rare interlayers in chlorite packets, but regular interstratifications characteristic of corrensite are absent. Fold profiles, as defined by the attitude of individual phyllosilicate crystallites, are disharmonic such that amplitude varies in successive fold profiles. Thus in Fig. 5(A) the core of the fold is open with a uniformly curved hinge, but successive profiles become tight and ultimately close in the envelope; fold limbs become straight and hinges abruptly angular. There is a noticeable absence of accommodation structures in the core, and profile lengths become greater towards the envelope when measured between two arbitrary lines parallel with and either side of the axial trace. The geometries therefore suggest progressive intracrystalline and grain boundary slip of phyllosilicates, parallel to (001), from core to envelope. The mechanism led to the development of triangular-shaped potential voids in the hinge zones which, as they tended to open, became filled with largely unstrained chlorite, as shown in the upper part of Fig. 5(B). These appear to be a nanometric equivalent of the microextensional sites illustrated by Knipe (1981). The chlorite defining the fold form shows a high density of defects (Fig. 5C). The most obvious are kinks representing the strain fields of dislocations resulting from slip parallel to (001). They closely resemble the edge and screw dislocations activated by basal slip in biotite and muscovite (Meike, 1989). Additional stacking defects caused by intercalation of extra 7-Å layers, as indicated by the 21-Å spacing in

A

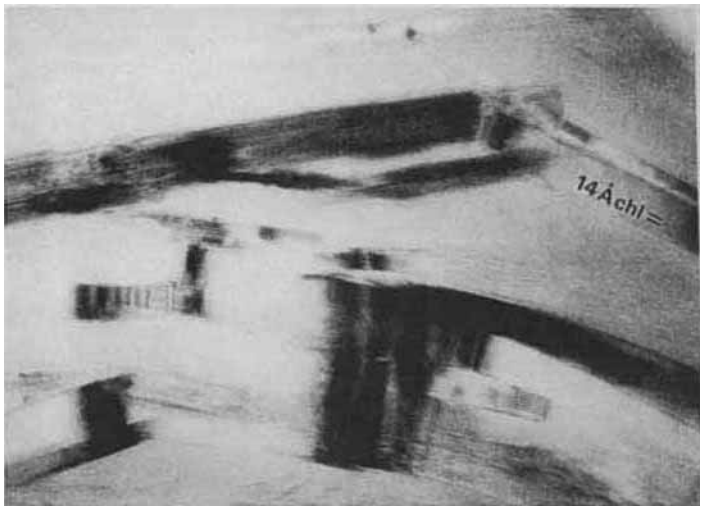

B

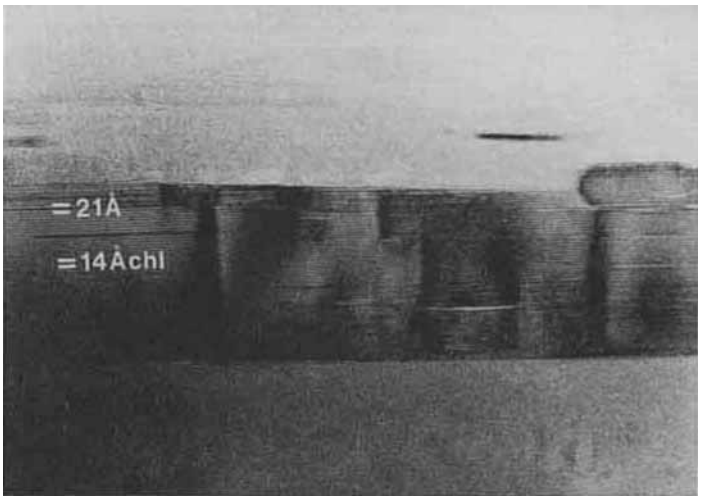

C

Fig. 5. TEM lattice fringe images of fabric-forming phyllosilicates in anchizonal slate sample BRS 444. (A) Nanometric-scale fold in intergrown chlorite and phengite crystallites showing strain-fields (kinks) resulting from dislocation by intracrystal slip on (001). (B) Hinge-line fracture in fold annealed by growth of chlorite crystallites along (001). (C) Polygonized chlorite crystal showing high density of defects, including dislocation slip along (001) with associated strain-fields (kinks), stacking defects and layer terminations.

Fig. 5(C), together with layer terminations, also appear to be associated with slip along (001). None of the phengitic micas imaged shows the high density of defects found in the associated chlorites, an observation similar to that recorded by Bons (1988) from Lower Palaeozoic slates in the Pyrenees.

TEM images of the epizonal slate sample BRS 106 show that the matrix phyllosilicates have a lower density of crystal defects than BRS 444 and few nanometric folds (Fig. 6A). By comparison with the two lower grade samples, intergrown chlorite and phengitic mica packets are straight, thicker and predominantly show low-angle grain boundaries subparallel to (001). High-angle chlorite/mica sutured boundaries as shown in Fig. 6(B) are uncommon. Passing from left to right across the boundary, the 14-Å fringes are flexed and appear to lose 7-Å fringes before passing into 10-Å fringes. Micas in BRS 106 are more prone to beam-damage mottling than chlorites, in contrast to the two previously described samples, where both phases easily became mottled in the electron beam. Mottling and fissuring in mica is mostly caused by beam-induced alkali migration, with the most marked fissures developing in paragonite (Ahn *et al.*, 1986; Merriman *et al.*, 1990; Shau *et al.*, 1991). Fissuring was not observed in any of the micas imaged for this study, consistent with the low Na contents determined by AEM (Table 2), and the absence of XRD-detectable paragonite. In BRS 106 the greater stability of chlorite to beam damage can be linked with a lower content of alkalis (Table 3) and the related absence of smectite interlayers.

Crystallite size

Size measurements were made on the photographic negatives of lattice-fringe images using a microfiche reader. Final magnifications of up to 6.4×10^6 could be achieved and allowed the two principal phyllosilicates present, 10-Å white mica and 14-Å chlorite, to be readily distinguished. Most measurements were made by counting regularly spaced 10- or 14-Å fringes parallel to c^*, between visible

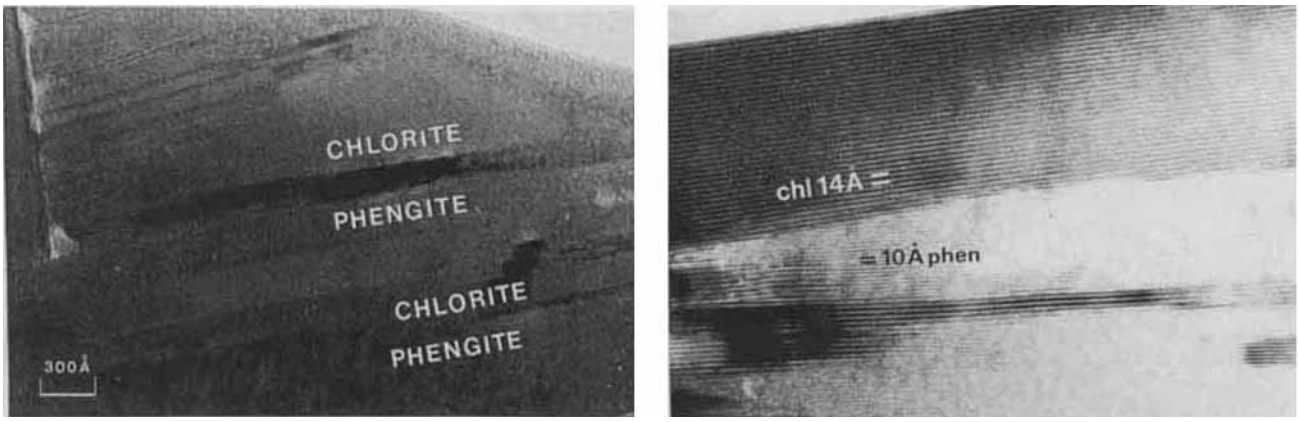

A B

Fig. 6. TEM lattice fringe images of fabric-forming phyllosilicates in epizonal slate sample BRS 106. (A) Intergrown chlorite and mottled phengitic white mica showing straight, low-angle grain boundaries. (B) Detail of a high-angle grain boundary between phengitic mica (phen) which transforms to chlorite, from right to left.

Table 1. TEM and XRD thickness measurements of phyllosilicate crystallites.

	TEM-measured white mica thickness			XRD-measured white mica thickness		TEM-measured chlorite thickness			XRD-measured chlorite thickness	
Sample no.	No. of crystallites measured	Mode (×10 Å)	Mean (×10 Å)	Effective crystallite thickness (×10 Å)	Kübler index (°2θ)	Number of crystallites measured	Mode (×14 Å)	Mean (×14 Å)	Effective crystallite thickness (×14 Å)	14-Å peak width (°2θ)
BRS 429	171	6.5	11.4	13	0.66 (1 s 0.02)	533	6	11.3	13	0.481 (1 s 0.04)
BRS 444	142	8.9	38.6	27	0.338 (1 s 0.006)	379	8	17.4	18	0.35 (1 s 0.01)
BRS 106	177	19.1	54.6	46	0.230 (1 s 0.004)	306	10	23.8	24	0.281 (1 s 0.01)
IOM 99	450	12	18.9	20	0.46 (1 s 0.02)	—	—	—	—	—

Table 2. Selected AEM analyses of white micas.*

	1	2	3	4	5	6	7	8
SiO_2	50.95	49.20	49.15	48.47	48.13	47.28	50.69	47.36
Al_2O_3	26.35	26.87	28.45	27.18	32.26	30.79	26.19	25.40
FeO†	6.26	6.80	5.92	2.13	1.61	2.61	3.01	3.99
MgO	2.09	1.60	1.57	4.94	2.43	2.98	4.27	5.64
Na_2O	0.58	0.00	0.00	0.57	0.72	0.55	0.00	1.82
K_2O	8.77	10.53	9.91	11.71	9.85	10.79	10.84	10.79
Sum‡	95.00	95.00	95.00	95.00	95.00	95.00	95.00	95.00
Number of cations normalized to 12 tetrahedral and octahedral cations								
Si	6.76	6.64	6.56	6.48	6.34	6.29	6.73	6.38
Al^{IV}	1.24	1.36	1.44	1.52	1.66	1.71	1.27	1.62
Al^{VI}	2.89	2.91	3.03	2.77	3.34	3.12	2.83	2.42
Fe^{2+}	0.70	0.77	0.66	0.24	0.18	0.29	0.33	0.45
Mg	0.41	0.32	0.31	0.99	0.48	0.59	0.84	1.13
Na	0.15	0.00	0.00	0.14	0.19	0.14	0.00	0.40
K	1.49	1.81	1.69	1.85	1.66	1.83	1.86	1.60
Total cations	13.64	13.81	13.69	13.99	13.85	13.97	13.86	14.00
Na/(Na + K)	0.09	0.00	0.00	0.07	0.10	0.07	0.00	0.20
Fe/(Fe + Mg)	0.63	0.71	0.68	0.20	0.27	0.33	0.28	0.29
mean b_0 (Å)§	9.044	9.040	9.034	9.038	9.020	9.024	9.044	

Analyses 1–3 diagenetic zone, BRS 429; analyses 4–6, anchizone, BRS 444; analyses 7–8, epizone, BRS 106. *2σ (from counting statistics) for Si: 0.03–0.05; Al: 0.01–0.02; Fe: 0.002–0.01; Mg: 0.006–0.02; Na: 0.01–0.03; K: 0.003–0.02. †All Fe calculated as FeO; ‡oxide wt% obtained by normalization of atomic ratios to 95.0 wt%; §Guidotti *et al.* (1989).

Table 3. Selected AEM analyses of chlorites.*

	1	2	3	4	5	6	7	8	9
SiO_2	33.78	36.10	30.05	26.78	28.37	34.35	28.16	27.55	24.87
Al_2O_3	17.27	17.81	18.21	20.82	18.59	19.55	20.79	19.34	20.34
FeO†	22.26	20.85	28.66	24.70	21.67	19.63	20.00	20.51	22.77
MgO	14.01	12.72	10.31	15.16	19.06	14.26	19.05	19.94	20.02
MnO	0.40	0.29	0.77	0.47	0.31	0.21	0.00	0.66	0.00
CaO	0.28	0.23	0.00	0.07	0.00	0.00	0.00	0.00	0.00
Sum‡	88.00	88.00	88.00	88.00	88.00	88.00	88.00	88.00	88.00
Structural formulae on the basis of 10 tetrahedral and octahedral cations									
Si	3.58	3.86	3.28	2.82	2.92	3.60	2.88	2.82	2.55
Al^{IV}	0.42	0.14	0.72	1.18	1.08	0.40	1.12	1.18	1.45
Al^{VI}	1.74	2.09	1.63	1.40	1.18	2.02	1.39	1.15	1.00
Fe^{2+}	1.98	1.86	2.62	2.18	1.87	1.72	1.71	1.75	1.95
Mg	2.22	2.03	1.68	2.38	2.92	2.24	2.90	3.04	3.05
Mn	0.03	0.02	0.07	0.04	0.03	0.02	0.00	0.06	0.00
Ca	0.03	0.02	0.00	0.01	0.00	0.00	0.00	0.00	0.00
Si/(Si + Al)	0.62	0.63	0.58	0.52	0.56	0.60	0.53	0.55	0.51
Fe/(Fe + Mg)	0.47	0.48	0.61	0.48	0.39	0.44	0.37	0.37	0.39
$Al^{VI}-Al^{IV}$	1.32	1.95	0.91	0.22	0.10	1.62	0.27	0.03	0.45

Analyses 1–3 diagenetic zone, BRS 429; analyses 4–6, anchizone, BRS 444; analyses 7–9, epizone, BRS 106. *2σ (from counting stastistics) for Si: 0.03–0.05; Al: 0.01–0.02; Fe: 0.002–0.01; Mg: 0.006–0.02; Mn: 0.01–0.02 Na: 0.01–0.03; K: 0.003–0.02. †All Fe calculated as FeO. ‡Oxides wt% obtained by normalization of atomic ratios to 88.0 wt%.

discontinuities in the sequence of layers. The following were regarded as discontinuities: grain boundaries between chlorite and mica; low-angle grain boundaries between subparallel packets of the same phase; high-contrast fringes with 10–12-Å spacings separating chlorite or mica packets, and probably representing collapsed smectite interlayers; tapering fringes in parallel sequences of fringes representing dislocations or stacking faults. Packets containing regular or random interstratifications of 10–12-Å layers (collapsed smectite) in chlorite were not measured, nor were single 10- or 14-Å layers. A given packet of mica or chlorite may be measured more than once if it contains, for example, layer terminations or internally coalescing smaller packets which are eliminated

normal to c^*. In terms of the Scherrer size, each defect-free thickness parallel to c^* acts as a coherent scattering domain in response to an incident X-ray beam, in contributing to the 'averaging' effect of diffraction.

Larger, defect-free crystallites of 50 or more fringes were measured with a ruler, having first calibrated the 10- and 14-Å periodicities for the microfiche magnifications used; errors introduced by this technique are $< \pm 5\%$. Phyllosilicates with crystallite thicknesses greater than the TEM field at 66×10^3, in effect those thicker than 1 μm, were not imaged. However, the thickest mica crystallite measured, 0.4 μm, was well inside this limit. Beyond an effective crystallite size $N_{(001)} = 100$ (10-Å layers), i.e. 0.10 μm thick, the Kübler index rapidly loses sensitivity (Merriman *et al.*, 1990).

Crystallite thickness data for white mica and chlorite are summarized in Table 1 and population distributions for the three samples are shown in Fig. 7. Kübler indices shown in Table 1 have been converted to the XRD effective crystallite size by means of the Scherrer expression and the corrections specified in Merriman *et al.* (1990, table 2). However, instead of the NBS 675 mica standard used in the latter work, instrument broadening was determined using a muscovite flake (Kisch, 1991), that gave a mean half-height width of 0.080 $\Delta°2\theta$ ($1\sigma = 0.001$) from 24 XRD scans across the 10-Å peak (Table 1). For similar chlorite thickness calculations, instrument broadening was determined from 14 XRD scans across the 14-Å peak of a single flake (1 cm^2) of clinochlore, which gave a mean half-height peak width of 0.081 $\Delta°2\theta$ ($1\sigma = 0.001$) using CuKα radiation. All XRD scans across 10- and 14-Å peaks employed the measuring conditions used in Kisch (1991).

In the diagenetic mudstone sample BRS 429, the white mica and chlorite populations have very similar mean

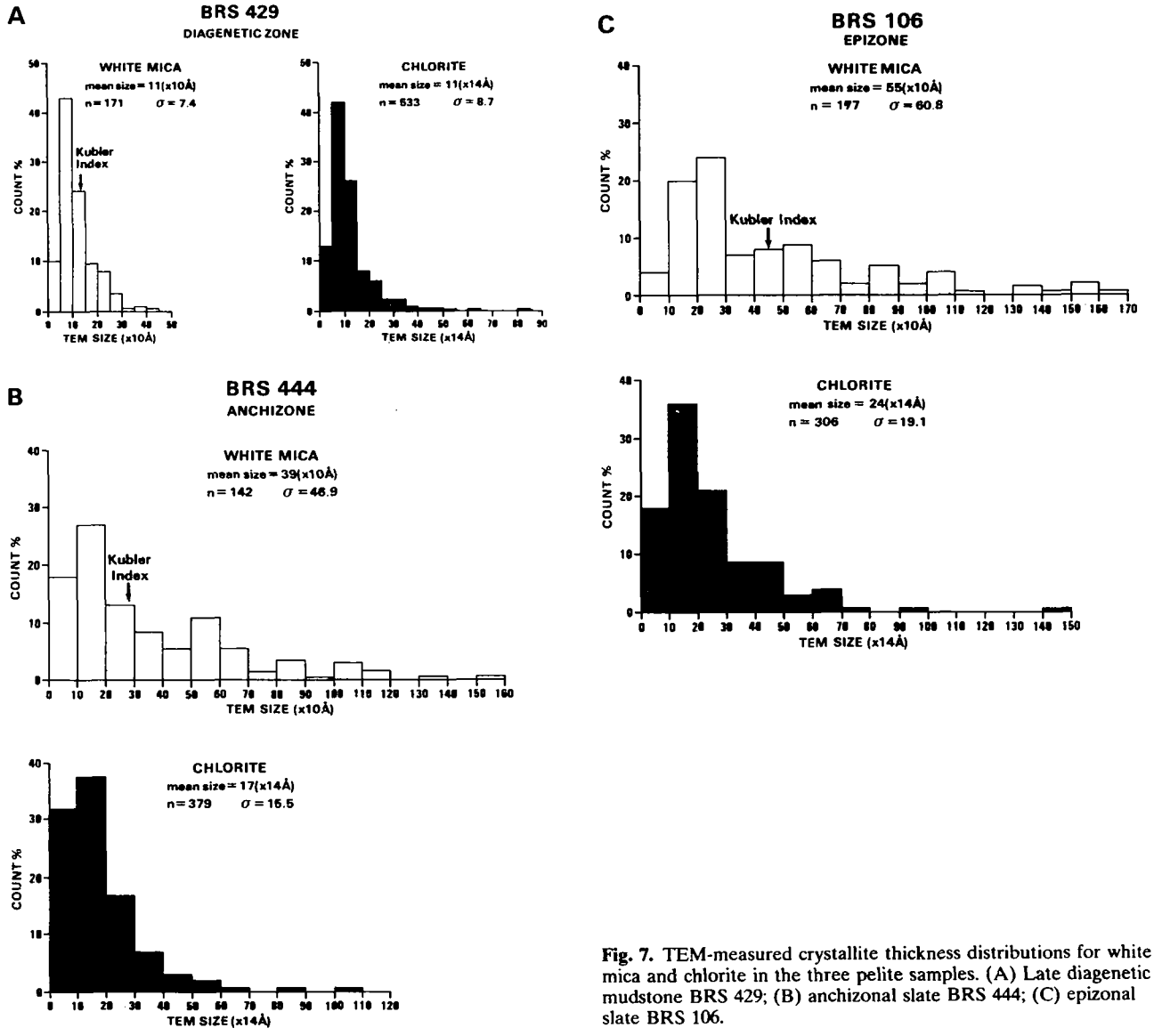

Fig. 7. TEM-measured crystallite thickness distributions for white mica and chlorite in the three pelite samples. (A) Late diagenetic mudstone BRS 429; (B) anchizonal slate BRS 444; (C) epizonal slate BRS 106.

thicknesses, 11.4 layers (114 Å) and 11.3 layers (158 Å), respectively, and both show similar distributions positively skewed towards larger sizes (Fig. 7A). Population modes are in the 5–10 layer interval for both phases (Table 1), and 95% of both populations have crystallite thicknesses of <25 layers. A mean Kübler index of 0.66 $\Delta°2\theta$ ($1\sigma = 0.02$) was determined from 24 XRD scans across the 10-Å peak of the <2-μm fraction of BRS 429, and converted to an effective crystallite thickness $N_{(001)} = 13$ (10-Å layers). A chlorite crystallinity index of 0.48 $\Delta°2\theta$ ($1\sigma = 0.04$) was derived from the mean half-height width of 11 XRD scans across the 14-Å peak, and converted to an effective crystallite thickness $N_{(001)} = 13$ (14-Å layers). It is clear from Table 1 that the TEM and XRD thicknesses for chlorite and mica in BRS 429 agree closely (Fig. 8).

In the anchizonal slate sample BRS 444, the thickness distributions for white mica and chlorite crystallites differ, although both are positively skewed towards larger sizes (Fig. 7B). The white mica population is distributed over a greater size range and appears to be polymodal, with 94% of crystallites possessing thicknesses of <100 layers for a population mean of 38.6 layers (386 Å). In contrast, the chlorite population shows a tighter distribution with 96% of crystallites having thicknesses of <50 layers for a mean thickness of 17.4 layers (244 Å). The effective crystallite thickness $N_{(001)} = 27$ (10-Å layers), derived from 24 XRD scans across the 10-Å peak of BRS 444, shows an approximate correlation with the mean, but not with the mode, of the TEM-measured white mica population (Table 1). The chlorite effective crystallite thickness $N_{(001)} = 18$ (14-Å layers), derived from 23 XRD scans across the 14-Å peak of BRS 444, shows good correlation with the TEM-measured mean of the chlorite population (Fig. 8).

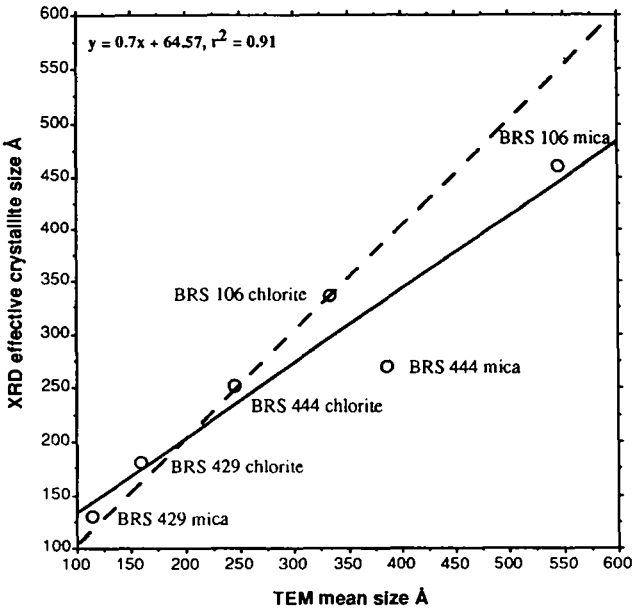

Fig. 8. Chlorite and white mica crystallite thickness data for the three pelite samples showing TEM mean size plotted against XRD effective size. Dashed line represents perfect correlation.

The epizonal slate sample BRS 106 also shows different distributions of white mica and chlorite size populations (Fig. 7C). White mica shows a polymodal distribution, with 95% of crystallites having thicknesses of <160 (10 Å) layers and a population mean of 54.6 layers (546 Å). The chlorite distribution is much tighter, with 94.5% of crystallites having thicknesses of <60 (14 Å) layers and a population mean of 23.8 layers (333 Å). White micas show an approximate correlation between the effective crystallite thickness $N_{(001)} = 46$ layers (460 Å), derived from 12 XRD scans across the 10-Å peak, and the mean of the TEM-measured white mica population (Table 1). Chlorite shows good correlation between the XRD-measured effective crystallite thickness $N_{(001)} = 24$ layers (336 Å), derived from 19 XRD scans across the 14-Å peak, and the TEM-measured mean thickness (Table 1).

Crystallite thickness data for the three samples are summarized in Fig. 8. Although the TEM and XRD measurements for both phases in sample BRS 429 correlate closely, as a result of their larger (001) spacing the mean size of chlorite crystallites is approximately 1.4 times greater than that of white micas. In contrast, the white mica population in sample BRS 444 shows a greater distribution than that of the chlorite population, and a mean thickness approximately 1.6 times greater than that of chlorite. Whereas the chlorite XRD- and TEM-measured mean thicknesses show good correlation in BRS 444, the corresponding white mica values show only approximate correlation. In sample BRS 106, again the chlorite population shows good correlation between TEM- and XRD-measured thicknesses, whereas that of white mica shows approximate correlation; the mean thickness of white mica is again 1.6 times greater than that of chlorite (Fig. 8). These data clearly show that, as grade increases, white mica crystals thicken more rapidly than chlorite crystals. The reduced correlation between white mica TEM and XRD measurements with increasing grade appears to be related to the more rapid growth of the micas. TEM measurements record the increase better than XRD because the latter has measured only those crystals retained in the <2-μm separations. The maximum thickness of crystals with an equivalent spherical diameter of 2 μm will depend on the aspect ratio diameter-to-thickness, which tends to vary from 40:1 in diagenetic grade mudrocks to 20:1 or less in epizonal rocks (Knipe, 1981; Merriman *et al.*, 1990). For a ratio of 20:1, very few mica crystals thicker than 0.1 μm, i.e. 100 (10 Å) layers thick would be expected in the <2 μm separation; this is close to the maximum thickness for crystallites making a contribution to the broadening (as opposed to the intensity) of the 10-Å peak profile (Merriman *et al.*, 1990). For a ratio of 10:1, few micas thicker than 0.2 μm would be expected in the <2-μm separation, but such crystals are recorded by TEM measurement. Hence there is a departure from good correlation between TEM and XRD measurements as crystal growth advances. Nevertheless, it is clearly the mean rather than the mode of the TEM-measured size population (Table 1) that most closely matches the XRD-measured crystallinity indices.

In a previous TEM study of white micas, a correlation was found between the TEM-measured mode of the population of crystallites and the XRD-measured effective crystallite thickness (Merriman *et al.*, 1990). Reservations were expressed by Merriman *et al.* (1990, p. 37) about the presence of paragonite in the samples studied and its possible effect of broadening the 10-Å peak profile, thus producing an apparently smaller effective crystallite thickness. Paragonite was not detected by XRD in the samples described here, and this suggests that paragonite, particularly homogeneous Na/K mica (Jiang & Peacor, 1993), previously regarded as regular mixed-layer paragonite/phengite (Frey, 1969), does indeed cause peak broadening, even where amounts do not exceed 20% of the <2-μm fraction.

Both the TEM- and XRD-measured crystal thicknesses indicate that white mica and chlorite crystals increase in size in response to metamorphism and the associated development of a tectonic fabric. The variations in mineral composition that accompany these prograde changes are detailed in the next section, where they are used to infer metamorphic temperatures and burial depths.

ANALYTICAL ELECTRON MICROSCOPY

Analyses were obtained from fabric-forming white mica and chlorite packets comprising continuous lattice fringes ranging from 50 Å to several hundred angstroms thick. Packets containing crystal defects or obvious interlayers, including corrensitic interlayers, were not analysed. Representative white mica analyses, shown in Table 2, are typically phengitic, with (Fe + Mg) in the range 0.66–1.58 per formula unit (pfu) and higher Si/Al ratios (6.29–6.73 Si pfu) than muscovite. Total interlayer cations (1.64–2.00) are within the range typical of evolved micas, consistent with the 2M polytypism revealed by SAED patterns. Low ratios of Na/(Na + K) are consistent with the general scarcity of XRD-detectable paragonite across the range of grades sampled. As grade advances, white micas become progressively less siliceous, with greater Al^{IV} substitution for Si, so that epizonal micas are generally the most Al-rich (Fig. 9). Analysed detrital white micas in late diagenetic mudstone sample BRS 429 are highly aluminous, with (Fe + Mg) = 0.40 and thus show typical muscovite compositions compared with the phengites that have evolved from the clay matrix.

Chlorite compositions show a series of prograde changes that can be related to the distribution of Al^{3+} and R^{2+}(Fe + Mg + Mn) in tetrahedral and octahedral sites (Table 3). The most siliceous chlorite, with the lowest R^{2+} contents and substantially more Al^{VI} than Al^{IV}, was found in the late diagenetic mudstone BRS 429. This chlorite, which is diabantite according to the scheme of Hey (1954), also commonly contains minor amounts of Ca, consistent with the presence of corrensite in BRS 429. By avoiding chlorite with obvious interlayered material, the analyses from BRS 429 show significantly lower total alkalis plus Ca than electron microprobe analyses of chlorites of

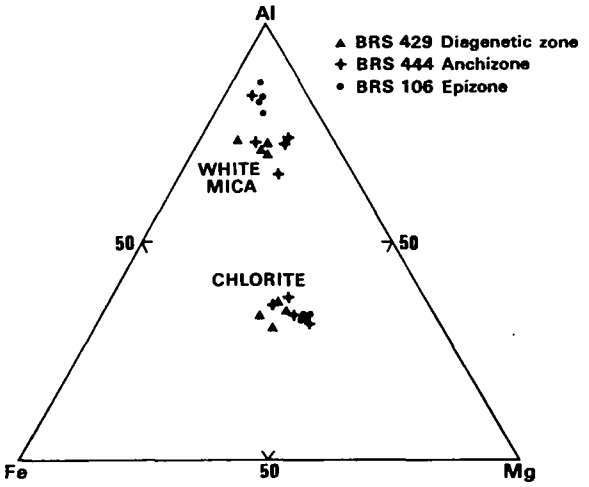

Fig. 9. Al–Fe–Mg diagram showing variations in matrix chlorite and white mica compositions in the pelite mudrock samples. Based on number of cations shown in Tables 2 & 3.

comparable grade, such as those from Zone 2 metabasites of Bevins *et al.* (1991) with quite different bulk rock compositions. Chlorite in the matrix of the anchizonal (BRS 444) and epizonal (BRS 106) slates is significantly less siliceous pycnochlorite and ripidolite, with higher R2 + contents and approximately equal amounts of Al^{VI} and Al^{IV}. Although variation in the ratio Fe/(Fe + Mg) is generally an indicator of chlorite precusor compositions (Bevins *et al.*, 1991), there is a trend towards lower ratios with increasing grade (Table 3), reflecting a prograde increase in Mg content (Fig. 9).

In summary, the compositional changes that occur in the fabric-forming phyllosilicates with advancing grade lead to a net decrease in Si content, together with minor decreases in Fe and Ca contents, a migration of alkalis from corrensite/chlorite to prograding white mica, and a mainly stoichiometric increase in Al and Mg in response to net losses.

Chlorite geothermometer

Variation in the Al^{IV} content and proportion of octahedral site vacancies of chlorites in meta-andesites has been inferred to be temperature dependent in hydrothermal systems (Cathelineau & Nieva, 1985). In relation to low-grade regional metamorphism, studies by Laird (1988) and Bevins *et al.* (1991) suggest that temperatures derived from the chlorite geothermometer can be correlated with those estimated from calcium–aluminium silicate assemblages in metabasic rocks. Although there is no evidence of chlorite formation in hydrothermal systems on the Rhins of Galloway, the temperature range covered by the chlorite geothermometer is very similar to that expected for the prograde sequence described here. However, in view of the reservations expressed by Jiang *et al.* (1994) on the validity of the geothermometer, temperatures derived from chlorite compositions (Fig. 10)

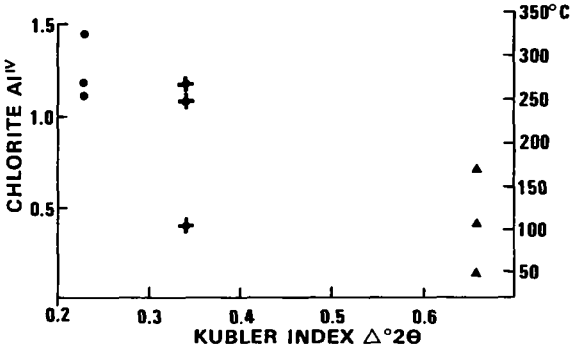

Fig. 10. Chlorite Al^{IV} contents plotted against Kubler index of coexisting white micas. The temperature scale on the right is derived from chlorite compositions in the Los Azufres geothermal system, after Cathelineau & Nieva (1985). Sample symbols as for Fig. 9.

must be treated with considerable caution. A plot of chlorite Al^{IV} against the Kubler index for the three samples (Fig. 10) shows a trend of increasing Al^{IV} with grade, but also shows considerable overlap in the range of values for each sample. A high smectite/corrensite content leads to low Al^{IV} when analyses are recast on the basis of the chlorite structure, hence the lowest temperatures derived from sample BRS 429 in Fig. 10 are unrealistic, whereas the maximum temperature of 170° C is reasonable for late diagenetic chlorite crystallization. Temperatures of 247 and 268° C derived from sample BRS 444 are within the expected range for the anchizone (Kisch, 1987), but a third value of 103° C is too low. Two values of 255 and 268° C are low for the epizone, whereas the maximum temperature of 325° C derived from sample BRS 106 is consistent with low epizone conditions. Further assessment of these temperatures is made in the Discussion, following the recommendations of De Caritat *et al.* (1993) that the geothermometer should be used only in combination with other temperature indicators.

K-white mica *b* parameters

The lattice parameter *b* of K-white micas has been used to characterize the 'baric type' and as a comparative geobarometer of the *P–T* gradient of low-grade metamorphic terranes (Sassi & Scolari, 1974). Variation in the magnitude of *b* results from an increase in the phengite content with increasing pressure involving the exchange $(Mg, Fe^{2+})^{VI} + Si^{IV} = Al^{VI} + Al^{IV}$ (Guidotti & Sassi, 1986). Measurement of *b* is normally made by XRD techniques, but the problems of separating and measuring matrix K-micas, as distinct from measuring a sample which includes detrital micas, has cast some doubt on the applicability of the technique to very low-grade pelitic rocks (Padan *et al.*, 1982). Regression equations relating cell dimensions of $2M_1$ muscovite to composition (Guidotti *et al.*, 1989) provided an alternative method to XRD, based on calculating *b* values from AEM data derived exclusively from non-detrital matrix K-micas. This method also overcomes the problem of interference from overlapping (060) and (331) XRD peaks noted by Huon *et al.* (1994).

Values obtained from paragonite-poor micas [Na/(Na + K) < 0.15] are shown in Table 2; each value is the mean of three calculations ($1\sigma = 0.01$) using the cell contents Σ (Mg, Fe), ΣAl and Si (Guidotti *et al.*, 1989). The *b* parameter does not appear to vary systematically with grade, so that the highest value of 9.044 Å is found in both the late diagenetic and the epizonal samples, whereas the lowest value of 9.020 Å is found in the anchizonal sample. It appears that *b* decreases with transition from the late diagenetic zone to the anchizone, despite the greater depth of burial inferred for the Shinnel Formation (Merriman & Roberts, 1993) represented by sample BRS 444. No significant change in bulk rock Fe/(Mg + Fe) ratios, as indicated by chlorite compositions in Table 3, accompanies the late diagenetic–anchizone transition, so that the decrease in *b* may be largely a response to increasing temperature (Velde, 1965). In an earlier study using XRD techniques, a trend of *b* increasing from diagenetic to anchizonal pelites was recorded in Kirkcudbright, Southern Uplands, by Kemp *et al.* (1985). The results presented here do not confirm such a trend, and suggest that a significant portion of the populations measured by XRD may have been poorly equilibrated, phengite-poor detrital micas. The transition from the anchizone to the epizone on the Rhins of Galloway is accompanied by an increase in *b* values, a trend similar to that recorded by Padan *et al.* (1982) from the Swedish Caledonides, using the conventional XRD method. However, more *b* values determined from AEM analyses of epizonal white micas are needed to confirm this trend in the Southern Uplands.

The mean value of 9.037 Å ($1\sigma = 0.010$), derived from 21 *b* calculations for the prograde sequence of white micas characterized here, indicates an intermediate pressure type, similar to that found in parts of the Scottish Dalradian (Fettes *et al.*, 1976) and the Otago terrane, New Zealand (Guidotti & Sassi 1986), both of Barrovian-type. This value is close to the highest mean value of 9.039 Å recorded from the intermediate-pressure facies series, and implies a field gradient of less than 25° C km^{-1} using the *P–T* curves of Guidotti & Sassi (1986; Fig. 1).

DISCUSSION

Crystal growth

Size distribution analysis of phyllosilicates in synthetic and natural systems (Baronnet, 1982; Eberl *et al.*, 1990) suggests that they may grow by Ostwald ripening, a process characterized by the simultaneous dissolution of smaller grains of a given mineral and growth of larger grains in a single medium (Ostwald, 1900). As ripening proceeds so the mean crystallite size increases, the number of crystallites decreases and the size distribution spreads out, whereas the level of supersaturation in the solution decreases. Ostwald ripening has been inferred in a prograde sequence of pelites from the Alps on the basis of

white mica thickness measurements made by the Warren–Averbach technique (Eberl *et al.*, 1990). When size distributions were plotted on reduced coordinates, obtained by dividing frequency values by the maximum frequency and crystallite thickness by mean thickness for each population, steady-state distributions were obtained. Normalized distributions of this type are independent of ripening time and initial size distribution, and have been used to characterize Ostwald ripening (Baronnet, 1982).

Crystallite thickness data derived from TEM measurements of the three samples are plotted on reduced coordinates in Fig. 11. The solid curve on each diagram is a calculated log-normal distribution, for an epizonal white mica population from the Alps (MF 998), showing a reduced profile characteristic of Ostwald ripening (Eberl *et al.*, 1990). In the diagenetic mudstone BRS 429, crystallite thicknesses of both chlorite and mica show log-normalized distributions which resemble those that characterize crystal growth by Ostwald ripening. Chlorite crystallite thickness data from the anchizonal (BRS 444) and epizonal (BRS 106) samples also resemble log-normal distributions, although the fit with curve MF 998 is poor compared with that shown by diagenetic chlorites in BRS 429. TEM evidence of abundant dislocations within the chlorites of BRS 444 and, to a lesser extent, BRS 106 suggests that as strain increased, chlorite crystal growth was less typical of Ostwald ripening processes. The white mica data from samples BRS 444 and BRS 106 show poor log-normal distributions and barely any resemblance to that of MF 998. It is surprising to find such poor correspondence with a typical Ostwald ripening curve, given the sparcity of TEM evidence of dislocations in the white micas.

The greater size and distribution range shown by white mica crystallites compared with chlorite crystallites in BRS 444 and 106 cannot be readily explained. If the disparity in size were related to the inclusion of size data from detrital micas this would lead to the strongest bimodality in the lowest grade sample BRS 429, but this is not so. Indeed, in this sample chlorite crystallites are generally larger than micas. Moreover, the good correlation between XRD-measured effective crystallite size, derived from <2-μm separations which exclude detrital micas, and TEM-measured mean size, indicates that the two independent techniques measured the same populations. The common occurrence of dislocations in chlorite compared with their paucity in mica offers a better explanation. Intracrystal basal slip parallel to (001) has the effect of reducing some of the larger chlorite crystallites to polygonized stacks of

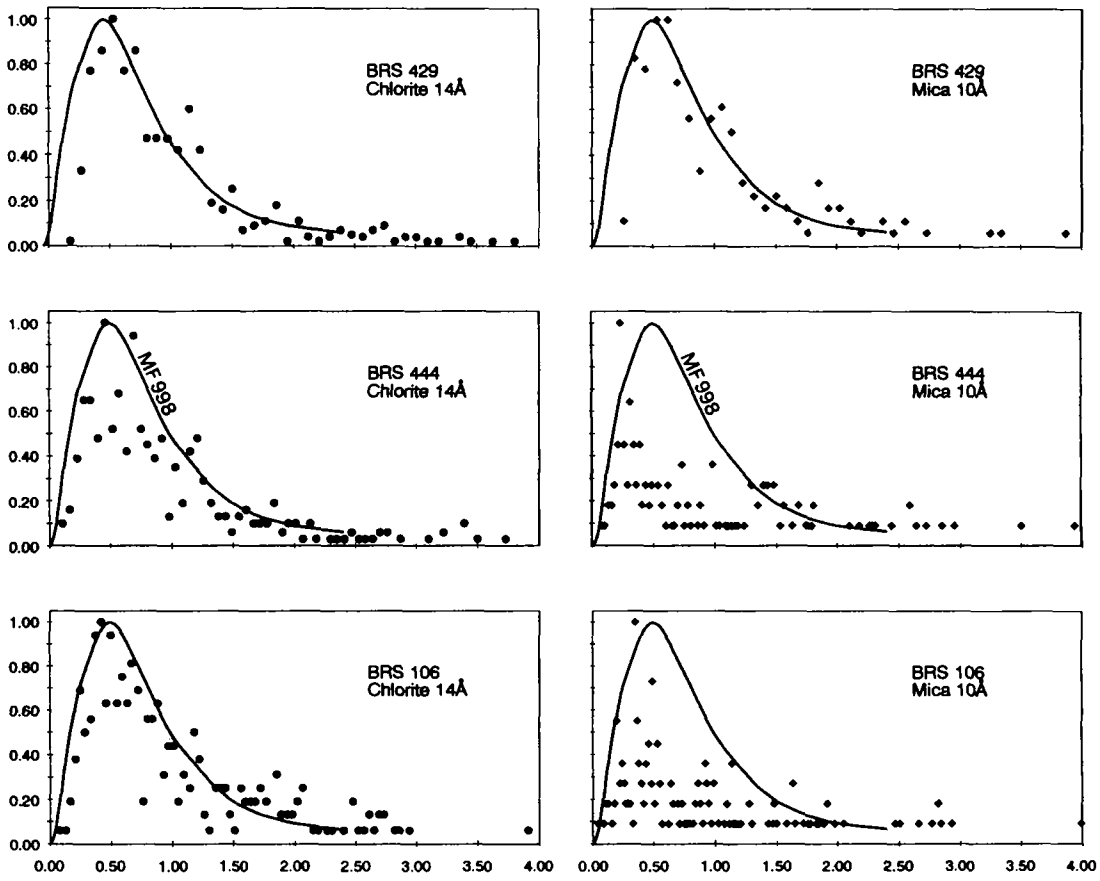

Fig. 11. Reduced coordinates plot of TEM-measured crystallite thickness data for the three pelite samples. The solid curve is the calculated log-normal distribution for an epizonal white mica population MF 998 from Eberl *et al.* (1990).

subgrains (Fig. 5C). These were treated as aggregates of crystallites for TEM measuring and also appear to have behaved as aggregates of coherently diffracting domains during XRD analysis. Clearly, the effect of basal dislocations is to reduce the mean thickness of the chlorite crystallite population compared with white micas, which were rarely observed as polygonized stacks. Since it is unlikely that the white mica closely intergrown with chlorite could have escaped deformation, it must respond to stress in some other way.

During shearing experiments at room temperatures Meike (1989) found that the screw dislocations that typically occur in muscovite were more difficult to activate than the more mobile edge dislocations typically found in biotite. Both types of dislocation are associated with the octahedral layer in these micas, where the dioctahedral nature of $2M_1$ muscovite favours screw dislocations which in turn require higher potential energies of dislocation compared with 1M trioctahedral biotite (Meike, 1989). At the higher temperatures associated with regional metamorphism, the stored strain energy associated with screw dislocations appears to promote more rapid grain-boundary migration in white micas compared with chlorite. Thus, in a TEM study of the development of slaty cleavage in the Pyrenees, Bons (1988) observed a high density of dislocations in chlorite whereas white mica was largely free of defects. Bons (1988) concluded that, because of its greater capacity to store elastic and plastic strain energy, mica tended to deform largely by grain-boundary migration whereas polygonization is a typical response for chlorite. These observations suggest that as white micas were stressed during deformation, dislocation activation was initially retarded but once activated subgrain development was recovered by grain-boundary migration and hence recrystallization. In contrast, the most common chlorite defect, caused by shifts of $b/3$ parallel to (001), has low stacking-fault energy (Bons & Schryvers, 1989) and is therefore less likely to promote recrystallization. As a result many chlorites retain strain-induced defects, because of the slow migration of dislocations (Urai *et al.*, 1986). Additionally, in the case of Southern Uplands chlorites, grain-boundary migration may have been inhibited by smectite interlayers inherited from corrensite. Discontinuous changes in the rate of grain-boundary migration would be expected as the Southern Uplands terrane evolved and may account for the polymodal thickness distributions (e.g. Urai *et al.*, 1986, p. 179) of the white micas in the more highly strained samples BRS 444 and BRS 106. White micas in these samples also show the greatest departure from typical Ostwald ripening profiles and it would seem that strain-induced crystal growth does not conform to the process described by Ostwald (1900).

The contrasting response to strain and related crystal growth observed in white mica and chlorite is reflected in the generally poor correlation between Kübler indices and chlorite crystallinity indices. Chlorite crystallinity indices for samples BRS 429, 444 and 106 fall within the diagenetic zone, anchizone and epizone, respectively, according to the zonal limits defined by Árkai (1991) using the chlorite crystallinity index $ChC_{(001)}$. Approximate correlation is found between the Kübler index ($IC_{(002)}$) and $ChC_{(001)}$ for the anchizonal slate, but very poor correlation exists between these indices for the diagenetic mudstone BRS 429 and the epizonal slate BRS 106, using Árkai's (1991) correlation. The present study suggests that in regionally metamorphosed terranes where deformation, fabric formation and crystal growth are closely associated, these two indices of phyllosilicate crystallinity can be expected to show a significant disparity. Relationships between the two indices is the subject of an ongoing TEM and XRD study.

Although subgrain development in white micas was not recorded in the Southern Uplands samples, our ongoing TEM studies show that elsewhere polygonization of white mica occurs in response to high strain rates. Intracrystalline deformation textures in a Lower Palaeozoic phyllonite from the Niarbyl shear zone, Isle of Man (Roberts *et al.*, 1990), are the result of intense comminution of the white micas (Fig. 12). Although the phyllonite is dominantly composed of strongly orientated 2M K- and Na-rich white micas, with rare chlorite, it possesses a white mica (illite) crystallinity index of 0.46 $\Delta°2\theta$, indicative of the late diagenetic zone (Table 1). TEM lattice fringe images show that white mica packets, originally 300–800 Å thick, are stacks of subgrains developed by strain-induced slip along (001). By XRD these are detected as a population of thin crystallites typical of a non-metamorphosed mudstone. Dislocations are marked by bands of reversed contrast normal to (001) which represent the strain fields associated with slip (Fig. 12). They resemble the screw dislocations produced in muscovite by Meike (1989). The polygonization of white micas occurred at high strain rates but the high structural level of the shear zone, with associated low temperatures

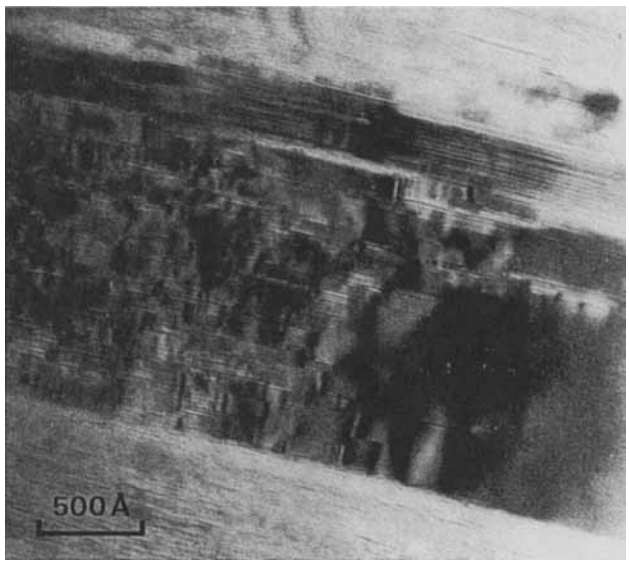

Fig. 12. TEM lattice fringe image of white mica in a phyllonite from the Niarbyl shear zone, Isle of Man. Intracrystal slip parallel to (001) is indicated by numerous dislocations with associated strain-fields (kinks) normal to (001).

(Roberts *et al.*, 1990), allowed very little post-shearing recovery. However, intense polygonization in the Niarbyl shear zone may also reflect relatively large grain thicknesses in an original slate or phyllite prior to shearing. As pointed out by Reitan (1977), stored strain energy is directly proportional to strain, but inversely proportional to grain size, and the rate of increase of stored strain energy is greater at low strain rates. Hence large grains at high strain rates store least strain energy. This evidence perhaps indicates that the absence of polygonized white micas from the Southern Uplands is related to lower or variable strain rates and/or smaller grain size, coupled with higher depth-related temperatures during imbrication. In the following section we explore how the conditions of regional metamorphism relate to phyllosilicate crystal growth in the Southern Uplands terrane.

Late diagenesis and very low-grade metamorphism

The accretionary prism model regards the Southern Uplands terrane as a succession of fore-arc sedimentary sequences sliced off an oceanic plate as it was subducted north-westwards beneath Laurentia (McKerrow *et al.*, 1977; Leggett *et al.*, 1979). Accretion developed under the toe of the SE-aggrading prism as a series of slices bounded by thrust faults dipping NW beneath the continental margin. As the prism developed, earlier accreted slices were steepened by backward rotation and acquired a pattern of very low-grade metamorphism related to burial (Oliver & Leggett, 1980; Oliver *et al.*, 1984). Phyllosilicate minerals in the sedimentary sequences have evolved in response to a series of prograde changes related to burial and fabric development associated with imbrication (Kemp *et al.*, 1985; Merriman & Roberts, 1993).

The lowest grade rocks in the Southern Uplands belong to the late diagenetic zone, represented by mudstone sample BRS 429. Rocks of this grade mainly crop out north of the Glen App Fault in the Corsewall Formation, and north of the Clanyard Bay Fault, in Gala tracts 7 and 8 (Fig. 1). Both outcrops are inferred to form upper units of a thrust stack (McCurry & Anderson, 1989; Merriman & Roberts, 1993). Mudstones and shales of this grade are possibly equivalent to the most deeply sampled shales in the Gulf Coast basin (Hower *et al.*, 1976; Eberl, 1994), but were probably more deeply buried. Moreover, many of the mineral reactions well documented from the Gulf Coast Basin (Peacor, 1992, and references therein) were probably accelerated by accretionary tectonism. For example, in the Barbados accretionary complex the initial stages of the smectite-to-illite transition are taking place at shallow depths, 500 m below the sediment–water interface, at temperatures of only 30° C. Neoformed illite crystallites are first observed below the décollement zone, where the early diagenetic changes are related to thrusting and enhanced fluid flow (Buatier *et al.*, 1992).

Similar conditions are likely to have promoted early diagenetic transformations in mudrocks as they were accreted in the Southern Uplands thrust system. During this stage the original ductile clay matrix, inferred to be predominantly saponitic because of the present high chlorite content, probably began to transform to corrensite and mixed-layer corrensite/chlorite, with scattered small domains of $1M_d$ illite. Bedding-parallel slip leading to bedding imbrication and stratal disruption during early accretion (Needham, 1993) most likely initiated nanometric-scale folding in the prograding matrix phyllosilicates. As the beds became progressively steepened and buried, further transformations of the matrix phyllosilicates with associated nanometric-scale folding would have occurred in response to bedding-parallel slip. At this stage much of the early diagenetic corrensite/chlorite and corrensite probably transformed to chlorite, while illite transformed to $2M_1$ phengitic white mica. The high phengite content of these micas resulted in large *b* spacings, indicative of a relatively low field gradient of $25° C km^{-1}$ or less, which is characteristic of an intermediate-pressure facies series. On the basis of the white mica and chlorite crystallinity values, these late diagenetic transformations almost certainly took place at temperatures below 200° C (Árkai, 1991). The occurrence of corrensite is consistent with such an upper temperature limit (Inoue & Utada, 1991), whereas the sporadic presence of kaolinite may indicate temperatures as low as 150° C (Kisch, 1987). Chlorite compositions, particularly the Al^{IV} contents (Fig. 10), indicate temperatures of up to 170° C, using problematic data derived from a geothermal system (Cathelineau & Nieva, 1985). Assuming temperatures in the range 150–200° C, a maximum field gradient of $25° C km^{-1}$ suggests that late diagenesis occurred at depths of at least 6–8 km.

Under these late diagenetic conditions, the crystal growth of chlorite appears to approximate to thickness distributions which are typical of Ostwald ripening, consistent with coalescence of thin chlorites initially separated by smectite layers. Stacking faults generated by dissolved smectite layers within a stack of chlorite crystallites may have provided the 'steps' which initiate spiral growth (Baronnet, 1982, 1992). Intracrystal slip would have provided additional dislocations for spiral growth, but perhaps low strain rates associated with early bedding imbrication of poorly lithified clays would tend to minimize stored strain energy in the prograding chlorite. Although white mica grew more slowly than chlorite, thickness distributions are also similar to typical Ostwald ripening curves and are consistent with growth by the $1M_d$ to $2M_1$ polytypic transformation (Baronnet, 1992). The resulting intergrowths of thin packets of chlorite and white mica in the matrix of BRS 429 closely resemble matrix textures seen in typical late diagenetic and some lower anchizonal mudstones in the Lower Palaeozoic Welsh Basin (Merriman *et al.*, 1990; Jiang *et al.*, 1990). Recent HRTEM/AEM studies by Li *et al.* (1994) indicate that such intergrowths developed through a series of prograde transitions in response to deep burial in the Welsh Basin. However, the nanometric-scale kinks and folds in these intergrowths seen in BRS 429 have not been observed in mudrocks that lack a tectonic fabric, implying that such

textures are perhaps related to the interaction between bedding-parallel slip and late diagenesis in imbricated sequences.

Anchizonal slates are widely developed in the Southern Uplands terrane (Oliver *et al.*, 1984: Kemp *et al.*, 1985), and on the Rhins of Galloway (Fig. 2), where they may have formed an underplated slate belt (Merriman & Roberts, 1993). Because of a tendency to be bedding-parallel, the tectonic fabric in these rocks is commonly inconspicuous; even in thin sections the anastomosing intergrowths of orientated white mica and chlorite forming the cleavage may be less obvious than detrital micas with the same orientation. However, the regional development of this fabric and the composition of the fabric-forming phyllosilicates (Tables 2 & 3), coupled with white mica crystallinity indices (Fig. 1), indicate that these rocks formed under higher grade conditions than those inferred for the late diagenetic zone. For example, a slight reduction in the phengite content of the white micas (Table 2) suggests growth at higher temperatures (Velde, 1965), compared with late diagenetic micas. Higher temperatures are also indicated by the increased Al^{IV} content of chlorites (Fig. 10), corresponding to a maximum of about 270° C, using the data of Cathelineau & Nieva (1985). Similar temperatures are commonly derived for mid-anchizonal conditions in other very low-grade terranes (Kisch, 1987; Roberts *et al.*, 1991). This temperature and a maximum field gradient of $25° C\,km^{-1}$ suggests that anchizonal metamorphism occurred at burial depths of at least 8–10 km and at temperatures 50–70° C higher than those inferred for late diagenetic strata.

Textures in sample BRS 444 suggest that the phyllosilicates developed in response to higher strain and more variable strain rates than those inferred from late diagenetic textures. Thus the crystallization of chlorite across fold hinge fractures (Fig. 5B) suggests that growth responded to different strain rates. High strain rates are indicated by crystal dislocations and brittle fractures, but where fractures are annealed by subsequent chlorite growth the crystals are strain-free, suggesting that recovery occurred at lower strain rates. At these higher grade conditions, the transformation of corrensite to chlorite appears to have been completed, but the relatively slow migration of dislocations generated by intracrystal slip inhibited recovery from subgrain development in many grains. Hence chlorite shows a narrower range of crystallite thicknesses and a smaller mean thickness than those of associated mica. The poor approximation to a typical Ostwald ripening curve (Fig. 11) perhaps indicates that screw dislocations propagating spiral growth may have been the main crystal growth mechanism. Intergrown phengitic white mica grew more rapidly than chlorite, increasing the mean thickness of the crystallite population by 2 or 3 times over that of the late diagenetic mica population. The elimination of smectite interlayers in chlorite and migration of alkali-bearing fluids derived from this reaction undoubtedly contributed to mica growth. However, much of this growth appears to be related to a greater capacity to store strain energy in the mica structure, leading to rapid migration of subgrain and grain boundaries once dislocations had been activated. The evidence from the Niarbyl shear zone (Fig. 12) clearly demonstrates the potential for subgrain development (polygonization) in white micas by activation of dislocations at high strain rates. We assume that if strain rates were high enough to cause brittle fracturing of nanometric fold hinges in BRS 444, then polygonization of white mica must also have occurred. The absence of these textures in the white micas from the Southern Uplands samples suggests that recovery from subgrain development at low strain rates was more effective than in associated chlorite. The marked departure of crystallite thickness distributions from typical Ostwald ripening curves (Fig. 11) is further evidence that crystal growth was primarily controlled by strain/recovery (annealing) processes rather than dissolution/recrystallization.

On the Rhins of Galloway, epizonal rocks are most widely developed in the thermal aureoles of late Silurian to early Devonian intrusions (Merriman & Roberts, 1993). An extensive area of regionally metamorphosed epizonal slate is found at the southern end of the Rhins peninsular in the Carghidown Formation (Figs 1 & 2), where a well-developed continuous cleavage is conspicuous in both pelites and interbedded greywacke sandstones. The compositions of fabric-forming phyllosilicates in the epizonal slate BRS 106 from this area are more evolved and indicative of higher temperatures than those in the anchizone. Phengitic micas are more aluminous, less siliceous and Mg-rich (Table 2), whereas chlorite compositions, particularly the Al^{IV} content (Fig. 10), also indicate higher temperatures, possibly up to 325° C according to the geothermometer of Cathelineau & Nieva (1985). Assuming a maximum field gradient of $25° C\,km^{-1}$, it would appear that epizonal conditions were attained at burial depths of at least 10–13 km in this part of the imbricate thrust terrane.

Textures in the fabric-forming phyllosilicates of the epizonal slate sample BRS 106 are characterized by a low density of crystal defects, few nanometric folds and relatively thick packets of chlorite and white mica (Fig. 6). Compared with the anchizonal slate (BRS 444), the mean crystallite thicknesses of chlorite and white mica are, respectively, 33 and 40% greater. Textures indicative of high strain rates are generally lacking, suggesting that the better developed slaty cleavage is largely the result of recovery (annealing) of both white mica and chlorite at low strain rates. Despite evidence of increased crystal growth by both phyllosilicates and a lower density of defects in chlorite crystals, epizonal conditions appear to sustain greater crystal growth rates in white mica compared with chlorite, as found in the anchizone. This suggests that the crystallite thickness distributions of both phases were inherited from a prograded anchizonal slate.

CONCLUSIONS

Differences in the crystal growth characteristics of the fabric-forming phyllosilicates in metapelites from the

Southern Uplands thrust terrane suggest that as grade increased tectonic strain played an important part in crystallization processes. Our observations suggest that during late diagenesis (150–200° C and 6–8 km depth), white mica and chlorite developed similar crystal growth patterns that resemble typical Ostwald ripening curves. These result from phase transitions in chlorite and corrensite and polytypic transformations in white mica. Under anchizonal conditions (<270° C and 8–10 km depth), tectonic strain resulted in differences in crystal growth. High strain rates promoted dislocations and subgrain development in chlorite crystals but recovery was inhibited by sluggish migration of subgrain boundaries at low strain rates. White mica crystals grew more rapidly than chlorite because of a greater capacity to store strain energy. As a result, dislocations which were activated at high strain rates migrated more rapidly at low strain rates than they did in chlorite, and thus annealed subgrains developed in mica crystals. In the epizone (<325° C and 10–13 km depth), low strain rates characterize the development of an intense slaty cleavage, and the greater thickness of white mica crystals compared with chlorite may have been inherited from the anchizone.

These observations specifically indicate that: (a) the strain-related crystal growth of white mica in the anchizone and epizone does not generate thickness distributions typical of Ostwald ripening; (b) both chlorite and mica XRD-measured crystallinity indices, converted to an effective crystallite size, generally correlate with the mean thickness of TEM-measured crystallite populations; (c) the crystallinity indices of white mica and chlorite are likely to show considerable differences in value where crystal growth is related to tectonic fabric development in low-grade metamorphic terranes.

ACKNOWLEDGEMENTS

We are grateful to P. Stone (BGS), who introduced us to the geology of the area. R. F. Symes (British Museum Natural History) and H. J. Kisch (University of the Negev, Israel) are thanked for supplying, respectively, the flake of clinochlore and the muscovite strip used as XRD standards. Reviews by P. Árkai, K. Brodie, D. D. Eberl and N. J. Fortey considerably improved earlier drafts of the manuscript. This work forms part of the BGS Southern Uplands Regional Geological Survey, and is published by permission of the Director, British Geological Survey (Natural Environment Research Council). TEM work was made possible and was supported by NSF grants EAR 91-04546 to D.R.P., and by a NATO Collaborative Research Grant No. CGR 920728.

REFERENCES

Ahn, J. H. & Peacor, D. R., 1986. Transmission and analytical electron microscopy of the smectite-to-illite transition. *Clays & Clay Minerals*, **34**, 165–186.

Ahn, J. H., Peacor, D. R. & Essene, E. J., 1986. Cation-diffusion-induced characteristic beam damage in transmission electron microscope images of micas. *Ultramicroscopy*, **19**, 375–382.

Árkai, P., 1991. Chlorite crystallinity: an empirical approach and correlation with illite crystallinity, coal rank and mineral facies as exemplified by Palaeozoic and Mesozoic rocks of north-east Hungary. *Journal of Metamorphic Geology*, **9**, 723–734.

Atherton, M.P., 1976. Crystal growth models in metamorphic tectonites. *Philosophical Transactions of The Royal Society of London, Series A*, **283**, 255–270.

Baronnet, A., 1992. Polytypism and stacking disorder. In: *Minerals and Reactions at the Atomic Scale: Transmission Electron Microscopy* (ed. Buseck, P. R.), *Mineralogical Society of America Reviews in Mineralogy*, **27**, 231–288.

Baronnet, A., 1982. Ostwald ripening in solution. The case of calcite and mica. *Estudios Geologicos*, **38**, 185–198.

Bell, I.A. & Wilson, C.J.L., 1981. Deformation of biotite and muscovite: TEM microstructure and deformation model. *Tectonophysics*, **78**, 201–228.

Bettison-Varga, L., Mackinnon, I. R. D. & Schiffman, P., 1991. Integrated TEM, XRD and electron microprobe investigation of mixed-layer chlorite–smectite from the Point Sal Ophiolite, California. *Journal of Metamorphic Geology*, **9**, 697–710.

Bevins, R. E., Robinson, D. & Rowbotham, G., 1991. Compositional variations in mafic phyllosilicates from regional low-grade metabasites and application of the chlorite geothermometer. *Journal of Metamorphic Geology*, **9**, 711–721.

Bons, A.-J., 1988. Intracrystalline deformation and slaty cleavage development in very low-grade slates from the Central Pyrenees. *Geologica Ultraiectina*, **56**.

Bons, A.-J. & Schryvers, D., 1989. High-resolution electron microscopy of stacking irregularities in chlorites from the central Pyrenees. *American Mineralogist*, **74**, 1113–1123.

British Geological Survey, 1992. *Rhins of Galloway*. Scotland Sheet 1 + 3 Solid, **1**, 50 000 Nottingham, British Geological Survey.

Buatier, M. D., Peacor, D. R. & O'Neil, J. R., 1992. Smectite–illite transition in Barbados accretionary wedge sediments: TEM and AEM evidence for dissolution/crystallization at low temperature. *Clays & Clay Minerals*, **40**, 65–80.

Cathelineau, M. & Nieva, D., 1985. A chlorite solid solution geothermometer. The Los Azufres geothermal system (Mexico). *Contributions to Mineralogy & Petrology*, **91**, 235–244.

De Caritat, P., Hutcheon, I. & Walshe, J. L., 1993. Chlorite geothermometry: a review. *Clays & Clay Minerals*, **41**, 219–239.

Eberl, D. D., 1994. Three zones for illite formation during burial diagenesis and metamorphism. *Clays & Clay Minerals*, **41**, 26–37.

Eberl, D. D., Srodon, J., Kralik, M., Taylor, B. E. & Peterman, Z. E., 1990. Ostwald ripening of clays and metamorphic minerals. *Science*, **248**, 474–477.

Fettes, D. J. Graham, C. M., Sassi, F. P. & Scolari, A., 1976. The basal spacing of potassic white micas and facies series variation across the Caledonides. *Scottish Journal of Geology*, **3**, 227–236.

Frey, M., 1969. A mixed-layer paragonite/phengite of low-grade metamorphic origin. *Contributions to Mineralogy & Petrology*, **24**, 63–65.

Frey, M., 1987. Very low temperature metamorphism of clastic sedimentary rocks. In: *Low Temperature Metamorphism* (ed. Frey, M.), pp. 9–58. Blackie and Son Ltd, Glasgow.

Guidotti, C. V. & Sassi, F. P., 1986. Classification and correlation of metamorphic facies series by means of muscovite bo data from low-grade metapelites. *Neues Jarbuch für Mineralogie Abhandlungen*, **153**, 363–380.

Guidotti, C. V., Sassi, F. P. & Blencoe, J. G., 1989. Compositional controls on the a and b cell dimensions of $2M_1$ muscovite. *European Journal of Mineralogy*, **1**, 71–84.

Hey, M. H., 1954. A new review of chlorites. *Mineralogical Magazine*, **30**, 277–292.

Hower, J., Eslinger, E.V., Hower, M. & Perry, E.A., 1976. Mechanism of burial metamorphism of argillaceous sediments: 1. Mineralogical and chemical evidence. *Geological Society of America Bulletin*, **87**, 725–737.

Huon, S., Burkhard, M. & Hunziker, J-C., 1994. Mineralogical, K–Ar, stable and Sr isotope systematics of K-white mica during very low grade metamorphism of limestones (Helvetic nappes, western Switzerland). *Chemical Geology (Isotopes Geoscience Section)*, **113,** 347–376.

Inoue, I. & Utada, M., 1991. Smectite-to-chlorite transformation in thermally metamorphosed volcanoclastic rocks in the Kamikita area, northern Honshu, Japan. *American Mineralogist*, **76,** 628–640.

Jiang, W-T. & Peacor, D. R. & Buseck, P.R., 1994. Chlorite geothermometry?-contamination and apparent octahedral vacancies. *Clays & Clay Minerals*, **42,** 593–605.

Jiang, W-T. & Peacor, D. R., 1993. Formation and modification of metastable intermediate sodium potassium mica, paragonite, and muscovite in hydrothermally altered metabasites from northern Wales. *American Mineralogist*, **78,** 782–793.

Jiang, W-T., Peacor, D. R., Merriman, R. J. & Roberts, B., 1990. Transmission and analytical microscope study of mixed-layer illite-smectite formed as an apparent replacement product of diagenetic illite. *Clays & Clay Minerals*, **38,** 449–468.

Kemp, A. E. S., Oliver, G. J. H. & Baldwin, J. R., 1985. Low-grade metamorphism and accretion tectonics: Southern Uplands terrain, Scotland. *Mineralogical Magazine*, **49,** 335–344.

Kisch, H. J., 1987. Correlation between indicators of very low-grade metamorphism In: *Low Temperature Metamorphism* (ed. Frey, M.), pp. 227–300. Blackie and Son Ltd, Glasgow.

Kisch, H. J., 1991. Illite crystallinity: recommendations on sample preparation, X-ray diffraction settings and interlaboratory standards. *Journal of Metamorphic Geology*, **9,** 665–670.

Knipe. R. J., 1981. The interaction between deformation and metamorphism in slates. *Tectonophysics*, **78,** 249–272.

Laird, J., 1988. Chlorites: metamorphic petrology. In: *Hydrous Phyllosilicates* (ed. Bailey, S. W.), *Mineralogical Society of America, Reviews in Mineralogy*, **19,** 405–453.

Leggett, J. K., McKerrow, W. S. & Eales, M. H., 1979. The Southern Uplands of Scotland: A Lower Palaeozoic accretionary prism. *Journal of the Geological Society, London*, **136,** 755–770.

Li, G., Peacor, D. R., Merriman, R. J. & Roberts, B., 1994. The diagenetic to low-grade metamorphic evolution of matrix white micas in the system muscovite-paragonite in a mudrock from central Wales, UK. *Clays & Clay Minerals*, **42,** 369–381.

Lorimer, G. W. & Cliff, G., 1976. Analytical electron microscopy of minerals In: *Electron Microscopy in Mineralogy* (ed. Wenk, H. R.), pp. 501–519. Springer-Verlag, New York.

McCurry, J. A. & Anderson, T.B., 1989. Landward vergence in the Lower Palaeozoic Southern Uplands-Longford-Down terrane, British Isles. *Geology*, **17,** 630–633.

McKerrow, W. S., 1987. Introduction: The Southern Uplands Controversy. *Journal of the Geological Society, London*, **144,** 735–736.

McKerrow, W. S., Leggett, J. K. & Eales, M. H., 1977. Imbricate thrust model of the Southern Uplands of Scotland. *Nature*, **267,** 237–239.

Meike, A., 1989. In situ deformation of micas: a high-voltage electron-microscope study. *American Mineralogist*, **74,** 780–796.

Merriman, R. J. & Roberts, B., 1993. The low grade metamorphism of Lower Palaeozoic strata on the Rhins of Galloway, SW Scotland. *Technical Report of the British Geological Survey*, **WG/92/40.**

Merriman, R. J., Roberts, B. & Peacor, D. R., 1990. A transmission electron microscope study of white mica crystallite size distribution in a mudstone to slate transitional sequence, North Wales, U K. *Contributions to Mineralogy & Petrology*, **106,** 27–40.

Needham.D. T., 1993. The structure of the western part of the Southern Uplands of Scotland. *Journal of the Geological Society, London*, **150,** 341–354.

Oliver, G. J. H., Smellie, J. L., Thomas, L. J., Casey, D. M., Kemp, A. E. S., Evans, L. J., Baldwin, J. R. & Hepworth, B. C., 1984. Early Palaeozoic metamorphic history of the Midland Valley, the Southern Uplands–Longford-Down massif and the Lake District, British Isles. *Transactions of the Royal Society of Edinburgh: Earth Science*, **75,** 259–273.

Oliver, G. J. H. & Leggett, J. K., 1980. Metamorphism in an accretionary prism: prehnite-pumpellyite facies metamorphism of the Southern Uplands of Scotland. *Transactions of the Royal Society of Edinburgh: Earth Science*, **71,** 235–246.

Ostwald, W., 1900. Über die vermeintliche Isomeric des roten und gelben Quecksilberoxyds und die Oberflächenspannung fester Körper. *Zeitschrift für physikalische Chemie Stochiometrie und Verwandtschaftslehre*, **34,** 495–503.

Padan, A., Kisch, H. J. & Shagam, R., 1982. Use of the lattice parameter b_0 of dioctahedral illite/muscovite, for the characterization of P/T gradients of incipient metamorphism. *Contributions to Mineralogy & Petrology*, **79,** 85–95.

Peacor, D. R., 1992. Diagenesis and low-grade metamorphism of shales and slates. In: *Minerals and Reactions at the Atomic Scale: Transmission Electron Microscopy* (ed. Buseck, P. R.), *Mineralogical Society of America Reviews in Mineralogy*, **27,** 335–380.

Rietan, P. H., 1977. Energetics of metamorphic crystallization. *Lithos*, **10,** 121–128.

Roberts, B., Morrison, C. & Hirons, S.R., 1990. Low grade metamorphism of the Manx Group, Isle of Man: a comparative study of white mica "crystallinity" techniques. *Journal of the Geological Society, London*, **147,** 271–277.

Roberts, B., Merriman, R. J. & Pratt, W., 1991. The influence of strain, lithology and stratigraphical depth on white mica (illite) crystallinity in mudrocks from the vicinity of the Corris Slate Belt, Wales: implications for the timing of metamorphism in the Welsh Basin. *Geological Magazine*, **128,** 633–645.

Sassi, F. P. & Scolari, A., 1974. The b_0 value of the potassic white micas as a barometric indicator in low-grade metamorphism of pelitic schists. *Contributions to Mineralogy & Petrology*, **45,** 143–152.

Shau, Y-H., Peacor, D. R. & Essene, E. J., 1990. Corrensite and Mixed-layer chlorite/corrensite in metabasalt from Northern Taiwan: TEM/AEM, EMPA, XRD and optical studies. *Contributions to Mineralogy & Petrology*, **105,** 123–142.

Shau, Y-H., Feather, M. E., Essene, E. J. & Peacor, D. R., 1991. Genesis and solvus relations of submicroscopically intergrown paragonite and phengite in a blueschist from northern California. *Contributions to Mineralogy & Petrology*, **106,** 367–378.

Sorby, H. C. 1853. On the origin of slaty cleavage. *New Philosophical Journal (Edinburgh)*, **55,** 137–148.

Stone, P., 1995. *The Geology of the Rhins of Galloway District.* Memoir of the British Geological Survey Sheet 1 + 3 (Scotland). HMSO for British Geological Survey, London.

Urai, J. L., Means, W. D. & Lister, G. S., 1986. Dynamic recrystallization of minerals. In: *Mineral and Rock Deformation: Laboratory Studies* (eds Hobbs, B. E. & Heard, H. C.), *The Paterson Volume. Geophysical Monograph*, **36,** 161–199.

Velde, B., 1965. Phengitic micas: synthesis, stability, and natural occurrence. *American Journal of Science*, **263,** 886–913.

Warr, L.N. & Rice, A. H.N., 1994. Interlaboratory standardization and calibration of clay mineral crystallinity and crystallite size data. *Journal of Metamorphic Geology*, **12,** 141–152.

White, S.H. & Knipe, R. J., 1978. Microstructure and cleavage development in selected slates. *Contributions to Mineralogy & Petrology*, **66,** 165–174.

Wilson, C. J. L. & Bell, I. A., 1979. Deformation of biotite and muscovite: optical microstructure. *Tectonophysics*, **58,** 179–200.

Received 15 November 1994; revision accepted 19 February 1995.